

JGR Solid Earth

RESEARCH ARTICLE

10.1029/2023JB027542

Effects of Pore Geometry and Saturation on the Behavior of Multiscale Waves in Tight Sandstone Layers

Jing Ba¹ , Rupeng Ma² , José M. Carcione^{1,3} , Ying Shi^{4,5,6}, and Lin Zhang¹ 

¹School of Earth Sciences and Engineering, Hohai University, Nanjing, China, ²Sanya Offshore Oil & Gas Research Institute, Northeast Petroleum University, Sanya, China, ³National Institute of Oceanography and Applied Geophysics—OGS, Trieste, Italy, ⁴School of Earth Sciences, Northeast Petroleum University, Daqing, China, ⁵Heilongjiang Provincial Key Laboratory of Oil and Gas Geophysical Exploration, Daqing, China, ⁶National Engineering Research Center of Offshore Oil and Gas Exploration, Beijing, China

Key Points:

- We investigate how fluid saturation affects wave attenuation and dispersion over a wide frequency range in tight sandstone layers
- A partial saturation model describes the fractal properties of the layers
- The size of the cracks and fluid patches are determined by applying the fractal model to the multiscale data

Correspondence to:

R. Ma,
marp@nepu.edu.cn

Citation:

Ba, J., Ma, R., Carcione, J. M., Shi, Y., & Zhang, L. (2023). Effects of pore geometry and saturation on the behavior of multiscale waves in tight sandstone layers. *Journal of Geophysical Research: Solid Earth*, 128, e2023JB027542. <https://doi.org/10.1029/2023JB027542>

Received 29 JUL 2023
Accepted 2 NOV 2023

Author Contributions:

Conceptualization: Jing Ba, José M. Carcione, Ying Shi
Data curation: Rupeng Ma
Formal analysis: Jing Ba, Rupeng Ma, José M. Carcione, Ying Shi
Funding acquisition: Jing Ba
Investigation: Jing Ba, Rupeng Ma, Lin Zhang
Methodology: Jing Ba, Rupeng Ma, José M. Carcione, Lin Zhang
Project Administration: Jing Ba, Rupeng Ma
Resources: Jing Ba, Rupeng Ma, Ying Shi
Software: Rupeng Ma, Lin Zhang
Supervision: Jing Ba, José M. Carcione, Ying Shi
Validation: Jing Ba, Rupeng Ma, José M. Carcione, Lin Zhang
Visualization: Rupeng Ma
Writing – original draft: Jing Ba, Rupeng Ma
Writing – review & editing: Jing Ba, José M. Carcione, Ying Shi, Lin Zhang

Abstract Geometric heterogeneities in tight reservoir rocks saturated with a fluid mixture may exhibit different scale distribution characteristics. Conventional models of rock physics based on poroelasticity, which usually consider single-scale pore structure and fluid patches, are inadequate for describing elastic wave responses. A major challenge is to establish the relationship between the wave response at different spatial scales and frequencies. To address this problem, three sets of observational data over a wide frequency range were obtained from a tight oil reservoir in the Ordos Basin, China. Ultrasonic measurements were made on eight sandstone samples at partial oil-water saturation at 0.55 MHz. Data from six borehole measurements and seismic profiles were acquired and analyzed at about 10 kHz and 30 Hz, respectively. Analysis of the cast thin sections shows that dissolution pores and microcracks generally develop, with fractal dimensions of the pores ranging from 2.45 to 2.67 for the samples with porosities between 5.1% and 10.2%. Compressional wave velocity and attenuation were estimated from the observed data. The results show that the velocity dispersion from seismic to ultrasonic frequencies is 10.02%, mostly occurring between sonic and ultrasonic frequencies. The attenuation is stronger at higher oil saturation. The relationships between velocity, attenuation, and wavelength were established and can be used for further forward modeling and seismic interpretation studies. A partial saturation model has been derived based on effective differential medium theory and a double double-porosity model, assuming that the medium contains fractal cracks and fluid patches. The effects of scale and saturation on wave responses are prevalent. Modeling results consistent with observed data show that the radii of cracks and fluid patches range from 0.1 μm to 2.8 mm, affecting ultrasonic, acoustic, and seismic attenuation. The multiscale data and proposed model quantify the relationship between fracture and fluid distributions and attenuation and could be useful for upscaling to the reservoir scale. The study helps improve the understanding of seismic wave propagation in partially saturated rocks, which has potential applications in seismic exploration, hydrocarbon production in reservoirs, and CO₂ sequestration in aquifers.

Plain Language Summary The physical properties of the rock and fluid can be inferred from the measured elastic wave responses and energy dissipation characteristics. However, the effects of heterogeneities of different sizes and at different frequencies can hinder studies to quantify wave responses in a partially saturated porous medium, which are usually based on laboratory measurements. A major problem is the difference between observed frequencies and scales: megahertz in the laboratory, 10 of kilohertz in the borehole scale, and hertz in the seismic exploration scale. In this work, the frequency- and saturation-dependent compressional velocity and attenuation are investigated using three geophysical data sets from the same tight reservoirs. A strong velocity dispersion over the measured frequency range is observed. The stronger attenuation at partial saturation may be caused by the multiscale heterogeneities of the pore structure and fluid patch distribution. A fractal poroelasticity model is developed by gradually inserting inclusions of different sizes with compliant pores and liquid patches into a homogeneous host skeleton. The wave responses are significantly affected by scale distribution and saturation. The proposed model, verified by the measured data, can be useful in interpreting the anelasticity of tight heterogeneous reservoirs in a broadband range.

1. Introduction

The petrophysical properties of rocks in the subsurface can be derived from elastic and seismic properties such as P-wave velocity and attenuation (e.g., Borgomano et al., 2019; Müller et al., 2010). Quantitative relationships

between these parameters can be established using in situ laboratory measurements and/or borehole data, which are essential for forward modeling and seismic interpretation geophysical studies. A key challenge is the upscaling of rock physics, going from the core or borehole scale to a larger scale (Dvorkin & Wollner, 2017). The pore geometry and fluid distribution typically observed at the core scale significantly affect the elastic and anelastic properties of the rock, especially in tight rocks (El-Husseiny et al., 2019; Ma et al., 2023). However, the effects of these heterogeneities at different spatial scales and frequencies have not been fully investigated in previous studies. Developing a poroelasticity model that accounts for multiscale heterogeneities and establishing a link between geophysical responses at different frequencies is critical. Such understanding may be insightful for oil and gas exploration and development, seismic monitoring of CO₂ storage, and gas storage site selection (Sokama-Neuyam et al., 2020; Wang et al., 2022; Zhong et al., 2023).

Ultrasonic experiments are conducted at higher frequencies (~MHz) than borehole (~kHz) and seismic surveys (~several tens of Hz). The presence of pore fluids can result in a large dispersion of wave velocity between different frequency bands. Numerous experimental studies have investigated the effects of fluid properties and saturation on rock velocity and attenuation. Some results indicate that pore fluid may be the main cause of wave attenuation (e.g., Best & Sams, 1997; Johnston et al., 1979; White, 1975; Winkler, 1985). Attenuation is generally higher in water-saturated rocks than in gas-saturated rocks (Adam et al., 2009; Kuteynikova et al., 2014; Toksöz et al., 1979; Winkler & Nur, 1982). Higher water saturations can lead to stronger wave loss in the partially saturated case such as gas and water (Amalokwu et al., 2014; Cadoret et al., 1998; Müller et al., 2008; Murphy, 1982; Yin et al., 1992). For example, the extensional loss of limestones is weak under dry and fully saturated conditions, but increases significantly at water saturation between 0%–20% and 95%–100% (Mikhailovitch et al., 2016). Q. Wei et al. (2021) indicated that partially saturated rocks with high clay content exhibit complex P-wave response characteristics, that is, attenuation is primarily influenced by the presence of gas, even at low saturation levels (about 5%), but permeability becomes a significant factor when gas saturation falls below 5%. Laboratory and modeling studies have shown that fluid viscosity is also related to velocity dispersion and attenuation (Chen et al., 2016; Yang et al., 2020). A decrease in viscosity shifts the attenuation curve to higher frequencies (Subramanian et al., 2015). The attenuation of seismic waves is controlled by the spatial distribution of the fluid (Chapman et al., 2017), which can be directly observed by injection experiments and CT imaging techniques (Lebedev et al., 2009; Lopes & Lebedev, 2012). Porous rocks can exhibit different attenuation properties at the same saturation level, which is due to the different fluid distribution resulting from the different saturation methods used in the experiments. Unlike gas-water saturation, the distinction between oil-bearing and water-bearing reservoirs remains quite difficult due to the similar fluid moduli, densities, and heterogeneities of fluid distribution. Understanding the saturation-dependent rock physics at different frequencies is important for improved fluid detection in heterogeneous reservoirs. Another challenge is the problem of scaling between laboratory core, borehole, and seismic data because heterogeneities of different sizes exist in actual rocks. Consequently, it can be difficult to ensure that rock physical properties obtained from centimeter-scale cores are representative of those in boreholes and seismic data (Bailly et al., 2019). Nevertheless, the variation trend of rock properties measured in the laboratory is believed to be applicable at large scale (Dvorkin & Nur, 2009; J. Li et al., 2020). To further investigate the scale effect, it is useful to obtain sufficient frequency-dependent data from the same geologic body.

Advances in poroelasticity theory have led to the recognition of wave-induced fluid flow (WIFF) as a general mechanism responsible for the acoustic wave velocity dispersion and attenuation (e.g., Ba et al., 2016; Carcione, 2022; Guo & Gurevich, 2020; Müller et al., 2010). Numerous models have been developed to simulate the wave responses at different fluid saturations (Ba et al., 2017; Chapman et al., 2016, 2017, 2021). Modeling results indicate that microscopic squirt flow, as well as mesoscopic and macroscopic fluid flow, can have significant effects at the different observation frequencies (Ba et al., 2011; Biot, 1956; Carcione, Poletto, & Farina, 2018; Carcione, Poletto, Farina, & Bellezza, 2018; Gurevich et al., 2010; Mavko & Nur, 1975). Wang et al. (2023) developed a fluid-saturated model incorporating microscopic, mesoscopic, and macroscopic heterogeneities and showed that the size of the inclusions significantly affects the attenuation. Similarly, M. Xu et al. (2022) derived a layered, partially saturated pore-crack model to study the effects of multiscale WIFFs. Ba et al. (2017) presented a double double-porosity model to analyze the mesoscopic and Biot fluid flows by simultaneously accounting for fabric and fluid heterogeneities. The reported models that consider heterogeneity of a single type and/or scale are insufficient to accurately describe the complex partially saturated porous media. It is also known that pore and fluid scale distributions in a subsurface medium can exhibit statistical self-similarity features (Feder, 1988; Katz & Thompson, 1985; Krohn, 1988). Several studies have simulated wave dissipation

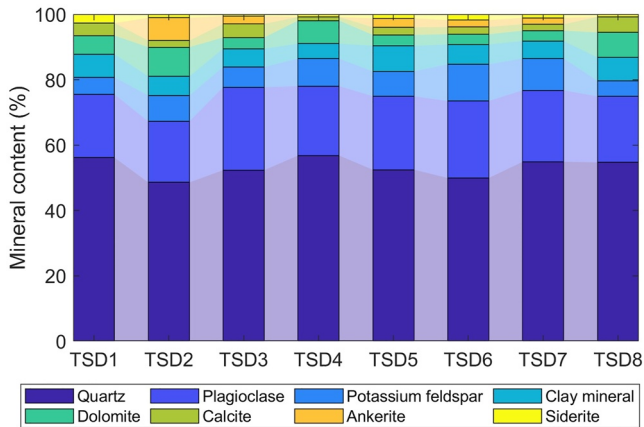


Figure 1. Mineral compositions and contents of the eight tight-rock samples.

in a saturated medium with fractal structures (Ma et al., 2023; Pride & Masson, 2006; L. Zhang et al., 2020), while others have resorted to partial saturation models to describe a medium in which the size of fluid patches follows an exponential or Gaussian distribution (Horikawa et al., 2021; Müller & Gurevich, 2004; Toms et al., 2007; L. Zhang et al., 2022). A more idealized model that accounts for the different scales with pore geometries and fluid distribution can then be expected. Further studies using extensive laboratory and field data are essential to promote the effective application of the theoretical model to actual seismic data.

In this work, we calculate compressional wave velocities and attenuation based on laboratory measurements, well logs, and seismic data from a tight oil reservoir in the Ordos Basin, China. Ultrasonic measurements were performed on eight tight sandstone samples partially saturated with oil and water under in-situ reservoir conditions. We analyzed the effects of rock properties, including porosity, clay mineral content, saturation, and pore distribution characteristics. Wavelength-dependent velocity and attenuation are analyzed by combining the multiscale data. A partial saturation model,

which assumes that the host skeleton contains a large radius range of inclusions with compliant pores and fluid patches, is developed and verified by using the multiscale data. Fractal properties of crack and fluid distribution in tight oil reservoirs are estimated.

2. Multiscale Data Acquisition

Multiscale geophysical data sets are obtained from the Chang 7 oil-bearing layer of the Mesozoic Triassic Yanchang Formation in the Ordos Basin, China. The Chang 7 layer, with a thickness of about 110 m, contains the widespread hydrocarbon source rocks of the basin. The sandstone and mud/shale formations consisting of multiple cycles with high interstitial content and rich natural fractures were formed as a result of gravity-driven sedimentation processes (H. Li et al., 2022). The sedimentary sand bodies are characterized by stable distribution and good continuity, and provide favorable reservoir conditions for large-scale oil accumulation. This study focuses on the fine-grained sandstone layer. The oil saturation is usually above 70%, with a maximum saturation of 90% under a strong driving force in a self-fed reservoir (Fu et al., 2020). Natural microscopic and macroscopic fractures are well-defined. Cracks are commonly observed in outcrops and cores of sandstone strata, which is a critical factor for oil accumulation. Statistical data from outcrop profiles show that cracks with openings of 0–1.5 mm account for 79.4% (Fu et al., 2020). Most cracks are not filled and form important channels for primary oil migration.

2.1. Lithofacies, Texture and Pore Types

Eight tight-rock samples of TSD1-TSD8 were collected from the fine-grained sandstone layer. Figure 1 shows their mineral compositions and contents, which are similar and consist mainly of quartz, feldspar, carbonate minerals, clay, and minor ore minerals, as determined by X-ray diffraction analyses. The quartz content varies from 48.59% to 56.81%. The feldspar minerals (mainly potassium feldspar and plagioclase) range from 24.53% to 34.76%, while the carbonate minerals (calcite and dolomite) range from 7.09% to 17.93%. The clay minerals account for 4.61%–7.84%.

Figure 2 shows the cast thin sections of samples TSD1-TSD8, numbered in ascending order of porosity. The analysis reveals the presence of three types of pores: intergranular pores, dissolution pores, and microcracks. The predominant pore types are feldspar dissolution pores and intergranular pores. Clay minerals are present to a lesser extent on grain surfaces. The microstructural properties of the samples are analyzed by using the image segmentation method, as shown in Figures 3a and 3c. For samples TSD1 and TSD8, the area porosities are 11.43% and 16.69%, while the probability density of cracks with aspect ratio less than 0.01 is 0.029 and 0.031, respectively. The probability density of stiff pores with aspect ratio of 1 is the highest at about 0.12, while those of the other aspect ratios mainly fall in the range of 0.02–0.42. Figures 3b and 3d show the histograms of probability density of pore diameter with self-similarity features. The fractal dimensions of the two samples are 2.67 and

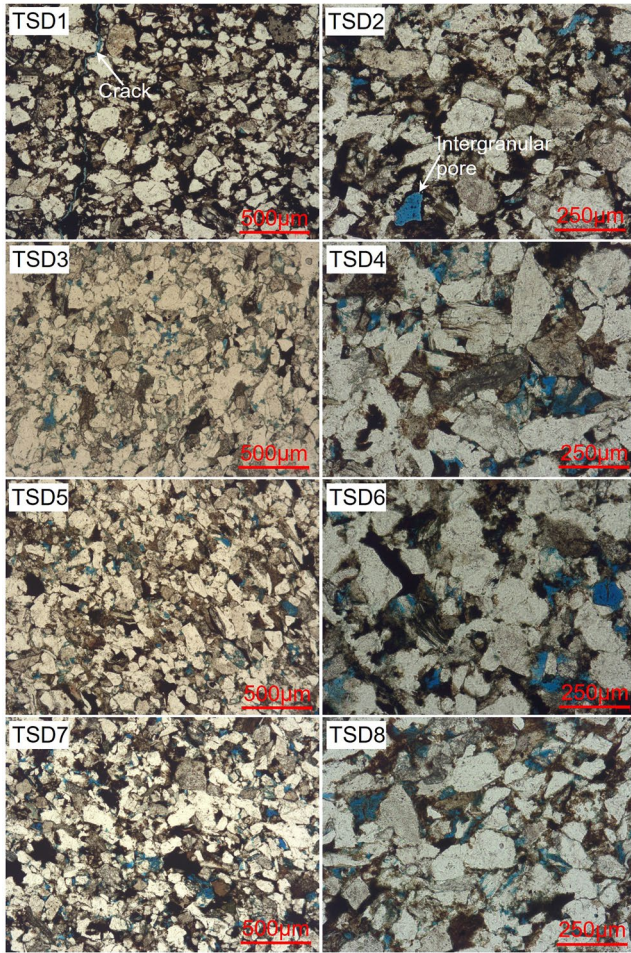


Figure 2. Casting thin section images of specimens TSD1–TSD8 at various magnifications. The blue areas denote the pores, while the black areas represent the interstitial material. The pore types are indicated.

2.45, when the histogram data are fitted by the probability density function in Yu and Li (2001). The pore diameters range mainly from 0.05 to 8 μm .

2.2. Laboratory, Well-Log and Seismic Observations

Laboratory measurements are performed on samples from the target reservoir at a depth of 1,800–2,122 m. The in-situ confining and pore pressures are about 30 and 15 MPa, respectively. The samples are cut into cylinders with a diameter of 25.20 mm and a length of 48.89–50.09 mm. Using the automatic permeameter of the core measurement system, we measure the porosities and permeabilities of the samples, which range from 5.1% to 10.2% and from 0.018 mD to 0.096 mD, respectively. Table 1 gives an overview of the properties of the samples.

The experimental apparatus in Ma and Ba (2020) is used to perform ultrasonic pulse velocity tests on the eight samples. The samples are saturated with water (brine) by using the vacuum-pressure saturation method. A rubber sleeve is used to isolate the cylindrical sample from the confining liquid. The sealed sample is then placed in a high-pressure vessel while brine is injected to control pore pressure. Ultrasonic waves are generated and received by two sensors at the ends of the sample. Compressional waveforms are recorded under in-situ conditions with a confining pressure of 30 MPa, a pore pressure of 15 MPa, and a temperature of about 30°C after we maintain the conditions for half an hour. For the oil-saturation and partial saturation measurements, the same procedures are repeated as for the water-saturation case with an increase in water saturation of about 20%. Each sample is first saturated with oil prior to the measurements. The oil saturation is then changed by using a drying oven and controlled by the weighting method (Ba et al., 2019), which can be estimated as follows

$$S_o = \left[1 - \frac{\Delta m \rho_{\text{sat}}}{m_{\text{sat}} \rho_{fo}} \left(\frac{1 - \phi}{\phi} \right) \right] \cdot 100\% \quad (1)$$

where m_{sat} , ρ_{sat} and ϕ are the mass, density and porosity of the water-saturated sample, respectively, Δm is the mass variation and ρ_{fo} is the oil density. Waveforms transmitting through an aluminum rod of the same shape as that of the sample (reference) are measured. The sampling

interval is 0.05 μs , while the transit time through the device is 8.35 μs when the two sensors are in direct contact. The pulse center frequency is 0.55 MHz. The P waveforms of sample TSD6 at different oil saturations are shown in Figure 4a. The velocity is obtained by dividing the sample length by the transit time through the sample. The error is calculated based on the uncertainty in the selection of the first arrival and the measurement of the length (Yurikov et al., 2018), which is 0.49% for sample TSD1 saturated with water. The attenuation coefficient γ is estimated based on the recorded sample and reference waveforms by using the spectral ratio method (Toksöz et al., 1979) as follows

$$\ln \left(\frac{A_1(f)}{A_2(f)} \right) = (\gamma_2 - \gamma_1)xf + \ln \frac{G_1(x)}{G_2(x)} \quad (2)$$

where $A(f)$ is the amplitude, f is frequency, x is the sample length, $G(x)$ is a geometrical factor, and the subscripts 1 and 2 refer to the sample and aluminum rod, respectively. The sample attenuation (inverse of quality factor Q) is $Q_1^{-1} = \gamma_1 V / \pi$, where V is the velocity. The amplitude spectrum is computed with one period of the signal after the first arrival to avoid the effect of boundary and multiple reflections. The attenuation uncertainty is calculated by the fitting error of the spectral ratio (Zhubayev et al., 2016). For example, the attenuation errors of sample TSD1 at water and oil saturations are 9.61% and 12.13%, respectively.

Log data from six wells were analyzed to determine the properties including density, porosity, gamma ray (GR), saturation, and velocity. Figure 5 shows the log curves of well C. The porosity of the reservoir ranges from

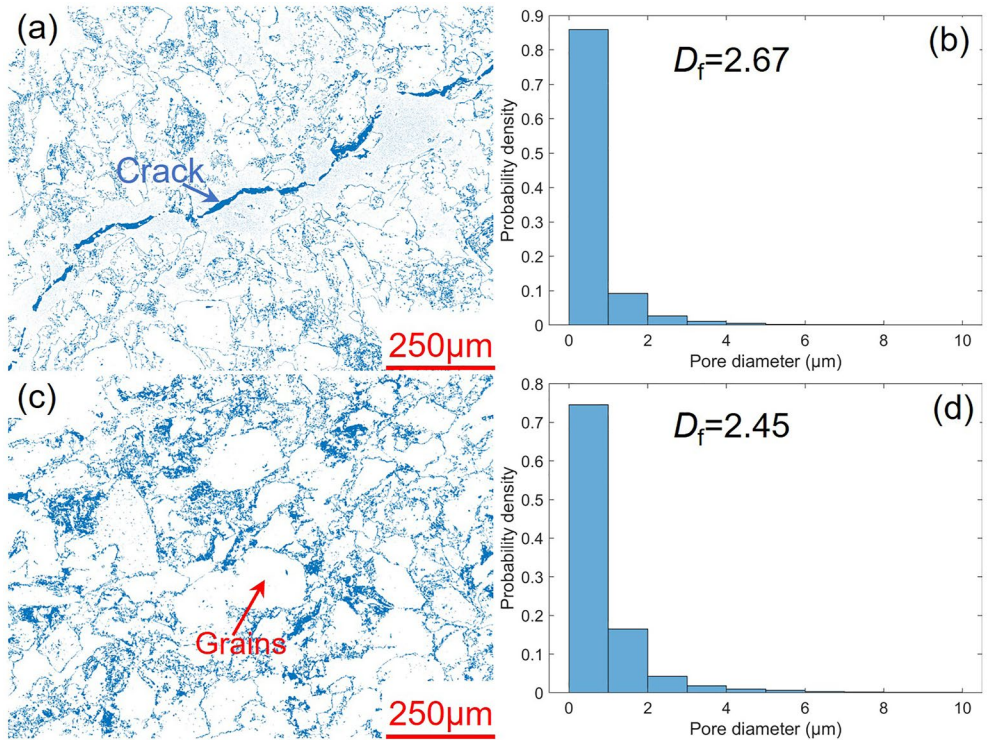


Figure 3. Microstructural properties of the specimens. (a, b) Show the distribution of pores (blue) and mineral grains (white) and the corresponding probability density histogram of pore diameter for sample TSD1; (c, d) are the corresponding information for sample TSD8. The fractal dimensions (D_f) of the pores are estimated.

0% to 11%. Water saturations range from 25% to 100%, with most ranging from 50% to 70%. The clay (shale) content curve derived from data at GR indicates that tight sandstone is predominant above a depth of 2,020 m. It is interbedded with mudstone layers, which are characterized by high clay content. Below this depth, mud/shale is the main lithology. The P-wave velocity ranges from 2,750 to 4,800 m/s. The analysis shows a strong correlation between P-wave velocity and porosity within the sandstone layer. Log data from the tight sandstone layer, characterized by low clay content, are selected for analysis and comparison with the experimental data. The full-waveform signals are recorded at 13 receivers with a spacing of 0.1524 m and a distance of 3.12 m from the source to the first receiver. Figure 4b shows the signals recorded at 2,030 m depth in Well C. The signals have a center frequency of about 10 kHz. The attenuation is estimated with the statistical average method (Sun et al., 2000),

$$Q_P(z) = \frac{\hat{\Phi}_n(z_0) - \hat{\Phi}_n(z) + Q_P^{-1}(z_0)t_n(z_0)}{t_n(z)} \quad (3)$$

where $\Phi_n = 2 \ln A_n(z, f)/f$, A_n is the n th receiver's spectrum, t_n is the propagation time, and z and z_0 denote the reservoir and reference depths, respectively. The Akaike information criterion algorithm is used to determine the arrival time of the P wave from the full-waveform data (Akram & Eaton, 2016). The attenuation is affected by the window length and spectral range. A time window of 120 μ s after the first arrival is used to extract one period of the signal, avoiding interference from S waves and multiple reflections between layers. The selected pulses are converted to amplitude spectra by using Fourier transform. The attenuation of the sonic log data is obtained by using a portion of the spectra near the center frequencies. Application of the statistical average method further increases the robustness of the attenuation estimate.

Table 1
Properties of Eight Tight-Rock Samples

Depth (m)	Sample	Porosity (%)	Permeability (mD)	Dry-rock density (g/cm ³)
1,997	TSD1	5.1	0.018	2.44
1,949	TSD2	5.8	0.020	2.51
2,012	TSD3	7.2	0.020	2.49
2,121	TSD4	9	0.078	2.41
1,994	TSD5	9	0.036	2.42
2,102	TSD6	9.2	0.038	2.44
1,800	TSD7	9.2	0.066	2.41
1,996	TSD8	10.2	0.096	2.37

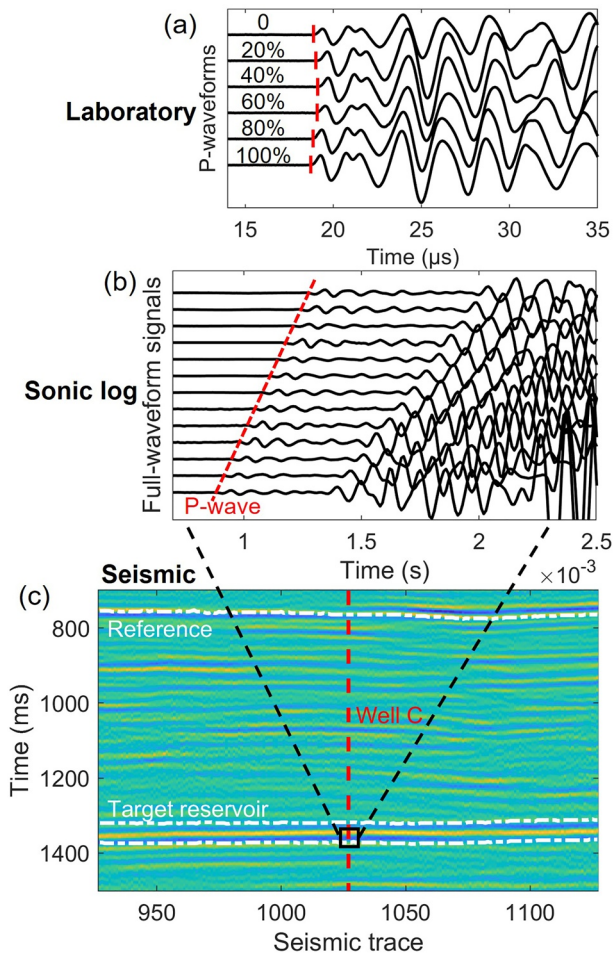


Figure 4. Waveforms recorded from ultrasonic measurements, sonic log and seismic observation. (a) P-waveforms of sample TSD6 and first arrivals (red lines) at different oil saturations. (b) Sonic-log signals recorded at 2,030 m depth from well C. First arrivals of P waves are indicated. (c) Seismic profile crossing well C.

crack, as is shown in Figure 3a. It is observed that attenuation increases with higher clay content. Additional energy dissipation could occur due to squirt flow between the intercrystal clay pores and the granular pores (Ba et al., 2016).

Figures 7 and 8 show the density distribution of velocity and attenuation data obtained from sonic log and seismic data. As porosity increases, velocity gradually decreases and attenuation increases. The velocities are mainly distributed in the range between 4.4 and 4.6 km/s, while the attenuation is mainly between 13 and 23. The seismic wave velocities are mainly in the range of 4.3–4.5 km/s, while the attenuation is between 24 and 27. The velocity and loss change significantly when the porosity is constant. This indicates the presence of strong heterogeneities, such as fractures and fluid patches, which may affect the wave responses. Some lithological variations may also effect on the scatters. The effect of fluid saturation on the velocity of tight-oil reservoirs is relatively small, compared to the velocity fluctuation observed in the sonic log data and seismic data presented in Figures 7 and 8.

3.2. Effects of Fluid Properties and Saturation

Figure 9 shows the P-wave velocities and attenuation of eight samples as a function of water saturation for partially oil- and water-saturated tests. The P-wave velocities initially decrease and then increase with water saturation, as observed for the first arrivals of sample TSD6 in Figure 4a. This trend differs from previous ultrasound

The seismic profile through the three wells in the study area is shown in Figure 4c. The thickness of the deposit is ~104 m, with porosity ranging from 2% to 12%. The shale layer has good continuity, indicated by the presence of a highly reflective interface. The seismic traces near the boreholes are used to determine the velocity and attenuation. The seismic velocity of the sandstone layer is determined by a pre-stack three-parameter inversion (Aki & Richards, 2002), while the attenuation is estimated by using an improved frequency shift method (Hu et al., 2013)

$$Q = \frac{\sqrt{\pi^5} t f_{c1} f_{c0}^2}{16(f_{c0}^2 - f_{c1}^2)}, \quad (4)$$

where f_{c0} and f_{c1} are the centroid frequencies of the reference and target layers, respectively, and t is the propagation time. The attenuation estimated from seismic data may be affected by the errors associated with seismic processing (migration, deconvolution, and frequency content), and it is locally dependent on the subsurface reflectivity (C. Zhang & Ulrych, 2002). A strong reflective interface above the target reservoir is considered as a reference in Figure 4c. The method eliminates the effects of the shape of the spectrum and noise and ensures a stable estimate. The generalized S-transform is used to perform a time-frequency analysis of the seismic data, which provides a suitable frequency resolution for identifying the interlayer information that is not identifiable by the short-time Fourier transform. The centroid frequency is approximately 30 Hz. Reservoir properties around the well, such as porosity, clay content, and saturation, are determined based on the corresponding log data.

3. P-Wave Velocity and Attenuation

3.1. Effects of Porosity, Permeability and Clay Content

The properties of eight samples are shown in Figure 6. Figure 6a shows a linear relationship between porosity and log of permeability, with dry density decreasing with increasing porosity. Figures 6b and 6c show the P-wave velocity (V_p) and attenuation ($1,000/Q_p$) of oil-saturated samples as functions of porosity and clay content, respectively. Velocities decrease with increasing porosity from 4.955 to 4.687 km/s, except for sample TSD1, which has an unusually low value. This deviation can be attributed to the presence of a

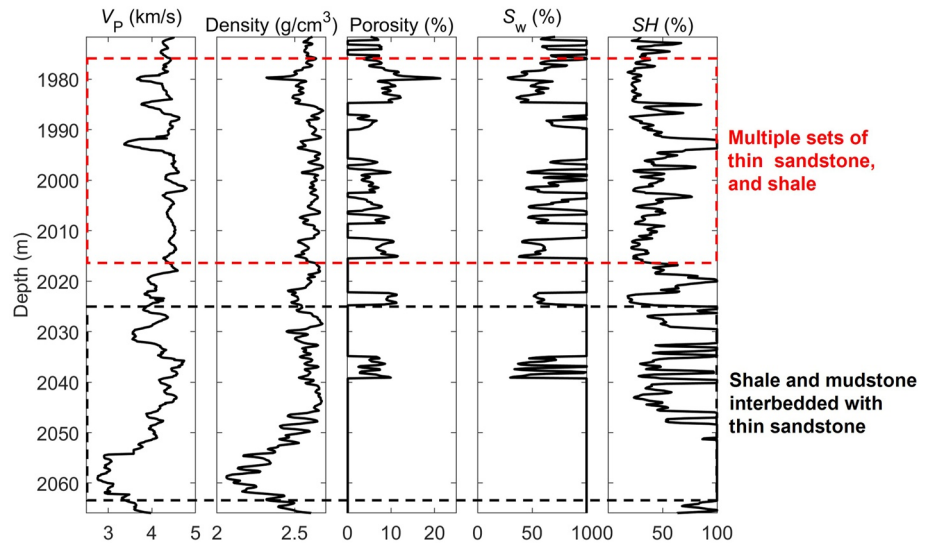


Figure 5. Log curves of well C, including P-wave velocity (V_p), density, porosity, water saturation (S_w), and shale content (SH) from left to right.

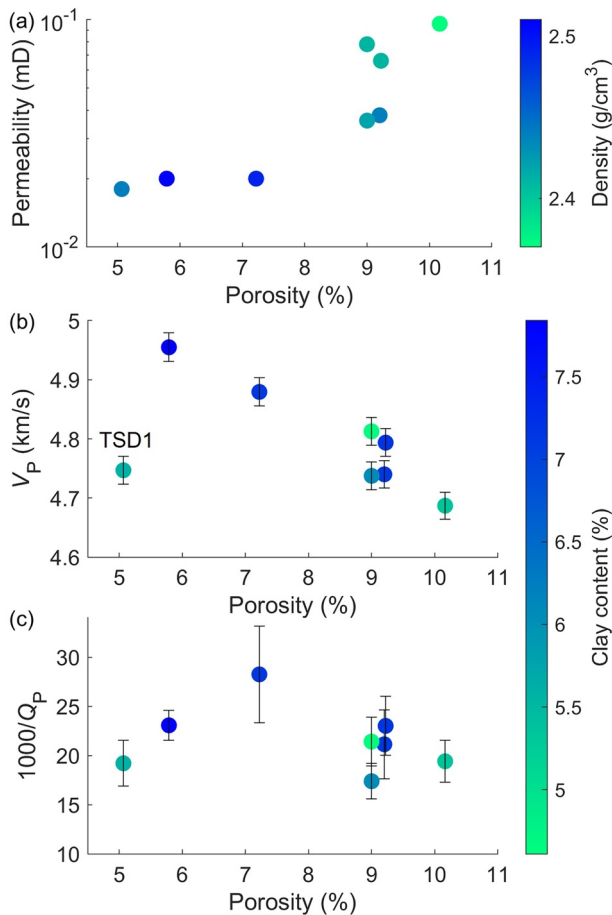


Figure 6. Relationships between the various properties of the eight samples. (a) Variations in porosity with respect to permeability and dry density. Variations in P-wave velocity (b) and attenuation (c) as a function of porosity and clay content in oil-saturated tests. Error bars are given.

measurements (e.g., Ma et al., 2021), which may be due to the complex fluid distribution properties in tight rocks (e.g., El-Husseiny et al., 2019). P-wave attenuation is stronger at partial saturation and generally peaks at high oil saturation due to the fluid flow induced by the waves at mesoscopic scale. The attenuation variation with saturation can also be affected by fluid distribution. Relative to the water-saturated condition, the maximum rates of velocity change with saturation range from 1.42% to 5.71% for different samples, with an average of 3.01%, while the maximum rates of attenuation change range from 7.95% to 47.07%, with an average of 23.75%. The attenuation attribute is very sensitive to changes in fluid saturation.

Figure 10 shows the sonic and seismic velocities and attenuation as a function of saturation and porosity. Both velocities increase with water saturation. Attenuation is generally stronger at partial saturation, suggesting that heterogeneities in fluid distribution may contribute to energy dissipation in addition to WIFF between stiff and compliant pores. Sonic and seismic data suggest that low porosity reservoirs generally have high water saturation, while high porosity reservoirs tend to have high oil saturation based on the available data.

3.3. Effect of the Wavelength

P-wave velocity and attenuation at the various observation scales are affected by factors such as measurement wavelength, saturation, porosity, and mineral content. The measured multiscale data sets under in-situ condition are shown in Figure 11. The P-wave velocity shows a strong scatter with frequency, while the attenuation appears to be stronger at relatively low frequencies. The sonic-log attenuation exhibits a wide distribution range due to the complex stratigraphic features and the selection of dense observation points.

Interpretation of geophysical data should be performed at the scale of the representative element volume. The transition from ultrasonic to seismic measurements involves a change in wavelength that significantly affects wave propagation in media with heterogeneities of different sizes. For a given lithology, velocity and attenuation measured at ultrasonic

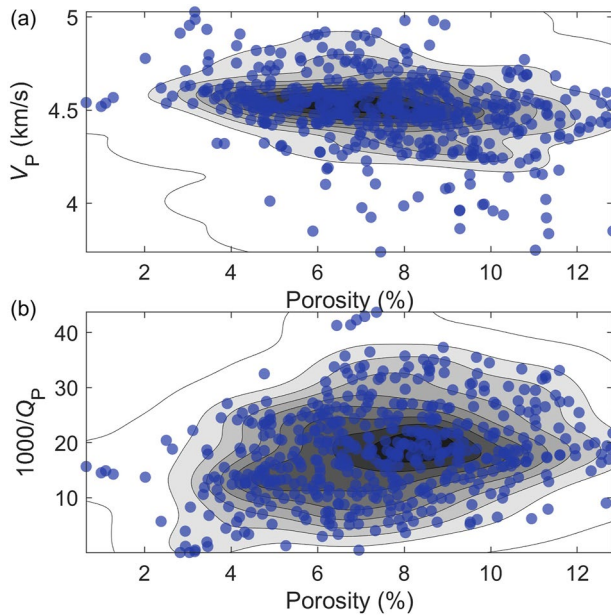


Figure 7. Density distribution of the P-wave velocity and attenuation obtained from the sonic log data.

structure (e.g., Horikawa et al., 2021). In this study, we assume that the pore-crack media are partially saturated with two immiscible fluids. The matrix with stiff pores (e.g., intergranular pores) serves as the host skeleton and contains a small volume of inclusions with compliant pores of different sizes (e.g., microcracks, cracks and fractures), as are shown in Figure 13. The host skeleton is assumed to be partially saturated while the inclusions are saturated. This is because the microcracks or grain contacts are usually saturated first due to capillary forces and water wettability of the interstitial material (X. Li et al., 2001). By assuming that the size distribution of spherical inclusions and fluid patches corresponds to statistical self-similarity, a fractal model for partially

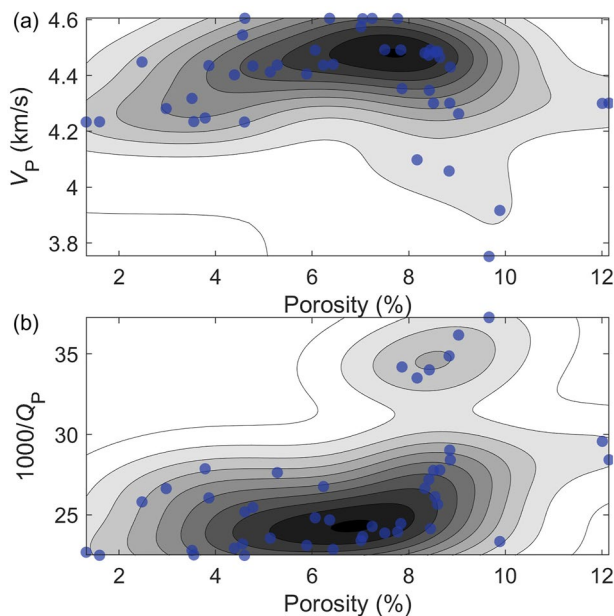


Figure 8. Density distribution of the P-wave velocity and attenuation obtained from the seismic data.

frequencies are governed by factors such as porosity, microstructure, and saturation, while reservoir properties obtained from sonic logs can be affected by fractures and interstitial material. Seismic properties are influenced by major heterogeneities such as fractures, stratification, and pelitic striations. Therefore, the variation in elastic and anelastic properties of multiscale data can reflect the heterogeneities at different spatial scales. Figure 12 shows descriptive statistics of the three velocity and attenuation data sets as a function of the measured wavelengths. The indicated are the median and quartiles of the data sets. The velocities decrease with increasing wavelength. The mean velocities decrease from 4.883 to 4.521 km/s as the wavelength increases from ~ 0.89 cm at the ultrasonic frequency to ~ 45 cm at the sonic frequency, with a velocity dispersion of about 8.02%. Mean velocities decrease slightly as the wavelength increases from ~ 45 cm to ~ 148 m at the seismic observation, with a velocity dispersion of about 2%. As the wavelength increases, the mean attenuation increases from 16.13 to 25.56.

4. A Fractal Model for Partially Saturated Pore-Crack Media

Pore structure and fluid distribution are considered typically fractal in shallow crusts and reservoir rocks. Previous fractal partially-saturated models of poroelasticity mainly analyze the patchy saturation of immiscible fluid mixture, but have not considered the heterogeneity within fabric/pore structure. In this study, we assume that the pore-crack media are partially saturated with two immiscible fluids. The matrix with stiff pores (e.g., intergranular pores) serves as the host skeleton and contains a small volume of inclusions with compliant pores of different sizes (e.g., microcracks, cracks and fractures), as are shown in Figure 13. The host skeleton is assumed to be partially saturated while the inclusions are saturated. This is because the microcracks or grain contacts are usually saturated first due to capillary forces and water wettability of the interstitial material (X. Li et al., 2001). By assuming that the size distribution of spherical inclusions and fluid patches corresponds to statistical self-similarity, a fractal model for partially saturated media can be proposed. Based on the differential effective medium theory, the additions of inclusions and fluid patches can then be divided into an infinite number of components with different radii and discretized into k values ($r_{I,1} > r_{I,2} > \dots > r_{I,k}$ and $r_{F,1} > r_{F,2} > \dots > r_{F,k}$) with a probability distribution. In the m th addition, a set of equal inclusions with volume $v_{I,m}$ and fluid patches with volume $v_{F,m}$ are embedded in the host skeleton, and form a triple-porosity system. It is assumed the medium porosity is ϕ , while the porosities of the host and inclusion are ϕ_H and ϕ_I , respectively. When the medium only contains stiff pores, the total porosity is $\phi = \phi_H$, and the inclusion porosity is $\phi_I = 0$. The host saturated with fluid 1 has an absolute porosity $\phi_{HF1,m} = (1 - v_{I,m})\phi_H S_{F1}$, while the host saturated with fluid 2 has an absolute porosity $\phi_{HF2,m} = (1 - v_{I,m})\phi_H S_{F2}$ and the inclusion saturated with fluid 1 has an absolute porosity $\phi_{IF1,m} = v_{I,m}\phi_I$, where S_{F1} and S_{F2} are the saturations of fluid 1 and 2 in the host, respectively, and $S_{F1} + S_{F2} = 1$. Fluid 1 and fluid 2 have the densities ρ_{F1} and ρ_{F2} , viscosities η_{F1} and η_{F2} , and bulk moduli K_{F1} and K_{F2} , respectively. The media can be considered as a simplified double double-porosity media (Ba et al., 2019) adding inclusions with radius r_I and incremental porosity $d\phi_I = \phi_I dv_I$, and adding fluid patches with radius r_F and incremental porosity $d\phi_{F2} = (1 - v_I)\phi_H dS_{F2}$ into the host skeleton. The strain energy of the considered media depends on the strains of the solid and fluid components based on Biot's theory. By including the relaxation effect of WIFF at the interfaces between different phases in the strain potential equation, the strain energy is obtained as follows (Ba et al., 2017),

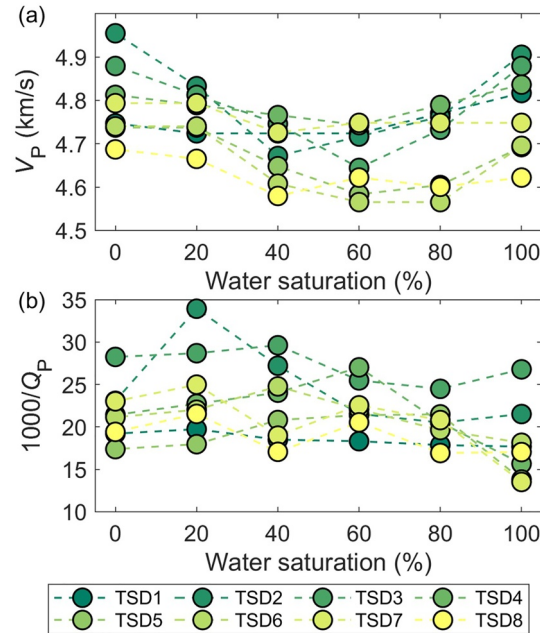


Figure 9. P-wave velocity (a) and attenuation (b) of eight samples as a function of water saturation.

$$\begin{aligned}
 2W = & (\tilde{A} + 2\tilde{N})I_1^2 - 4\tilde{N}I_2 \\
 & + 2\tilde{Q}_1I_1[\xi_{H1} + \zeta_{H1I1}\phi_I dv_I + \zeta_{H1H2}(1 - v_I)\phi_H dS_{f2}] \\
 & + \tilde{R}_1[\xi_{H1} + \zeta_{H1I1}\phi_I dv_I + \zeta_{H1H2}(1 - v_I)\phi_H dS_{f2}]^2 \\
 & + 2\tilde{Q}_2I_1[\xi_{I1} - (1 - v_I)\phi_H \zeta_{H1I1}] + \tilde{R}_2[\xi_{I1} - (1 - v_I)\phi_H \zeta_{H1I1}]^2 \\
 & + 2\tilde{Q}_3I_1[\xi_{H2} - (1 - v_I)\phi_H S_{f1}\zeta_{H1H2}] + \tilde{R}_3[\xi_{H2} - (1 - v_I)\phi_H S_{f1}\zeta_{H1H2}]^2
 \end{aligned} \tag{5}$$

where I_1 and I_2 are the first and second strain invariants, and ξ_{H1} , ξ_{I1} , and ξ_{H2} are the displacement divergence fields of fluid 1 in the host, fluid 1 in the inclusions and fluid 2 in the host, respectively. The scalars ζ_{H1I1} and ζ_{H1H2} denote the fluid strain increments at the interfaces between the host and inclusion saturated with fluid 1 and between the hosts with fluid 1 and fluid 2, respectively. The analytical relations between the stiffness coefficients and the measurable properties of the rock and fluid can be derived by the method of gedanken experiments (Johnson, 1986). The unjacketed rock is subjected to both pure shear deformation and hydrostatic pressure based on the idealized experiments (Ba et al., 2011). The stiffness coefficients are

$$\begin{aligned}
 \tilde{N} &= \mu_b, \\
 \tilde{A} &= (1 - \phi - d\phi_I)K_s - \frac{2}{3}\tilde{N} - \tilde{Q}_1\frac{K_s}{K_{f1}} - \tilde{Q}_2\frac{K_s}{K_{f1}} - \tilde{Q}_3\frac{K_s}{K_{f2}}, \\
 \tilde{Q}_1 &= \frac{\beta(1 - \phi - d\phi_I - K_b/K_s)(1 - v_I)\phi_H S_{f1}K_s}{\beta(1 - \phi - d\phi_I - K_b/K_s) + K_s/K_{f1}[\beta(1 - v_I)\phi_H + \phi_I dv_I]}, \\
 \tilde{Q}_2 &= \frac{(1 - \phi - d\phi_I - K_b/K_s)K_s\phi_I dv_I}{(1 - \phi - d\phi_I - K_b/K_s) + K_s/K_{f1}[\beta(1 - v_I)\phi_H + \phi_I dv_I]}, \\
 \tilde{Q}_3 &= \frac{\beta(1 - \phi - d\phi_I - K_b/K_s)K_s(1 - v_I)\phi_H dS_{f2}}{\beta(1 - \phi - d\phi_I - K_b/K_s) + K_s/K_{f2}[\beta(1 - v_I)\phi_H + \phi_I dv_I]}, \\
 \tilde{R}_1 &= \frac{[\beta(1 - v_I)\phi_H + \phi_I dv_I](1 - v_I)\phi_H S_{f1}K_s}{\beta(1 - \phi - d\phi_I - K_b/K_s) + K_s/K_{f1}[\beta(1 - v_I)\phi_H + \phi_I dv_I]}, \\
 \tilde{R}_2 &= \frac{[\beta(1 - v_I)\phi_H + \phi_I dv_I]K_s\phi_I dv_I}{(1 - \phi - d\phi_I - K_b/K_s) + K_s/K_{f1}[\beta(1 - v_I)\phi_H + \phi_I dv_I]}, \\
 \tilde{R}_3 &= \frac{[\beta(1 - v_I)\phi_H + \phi_I dv_I]K_s\phi_I dv_I(1 - v_I)\phi_H dS_{f2}}{\beta(1 - \phi - d\phi_I - K_b/K_s) + K_s/K_{f2}[\beta(1 - v_I)\phi_H + \phi_I dv_I]},
 \end{aligned} \tag{6}$$

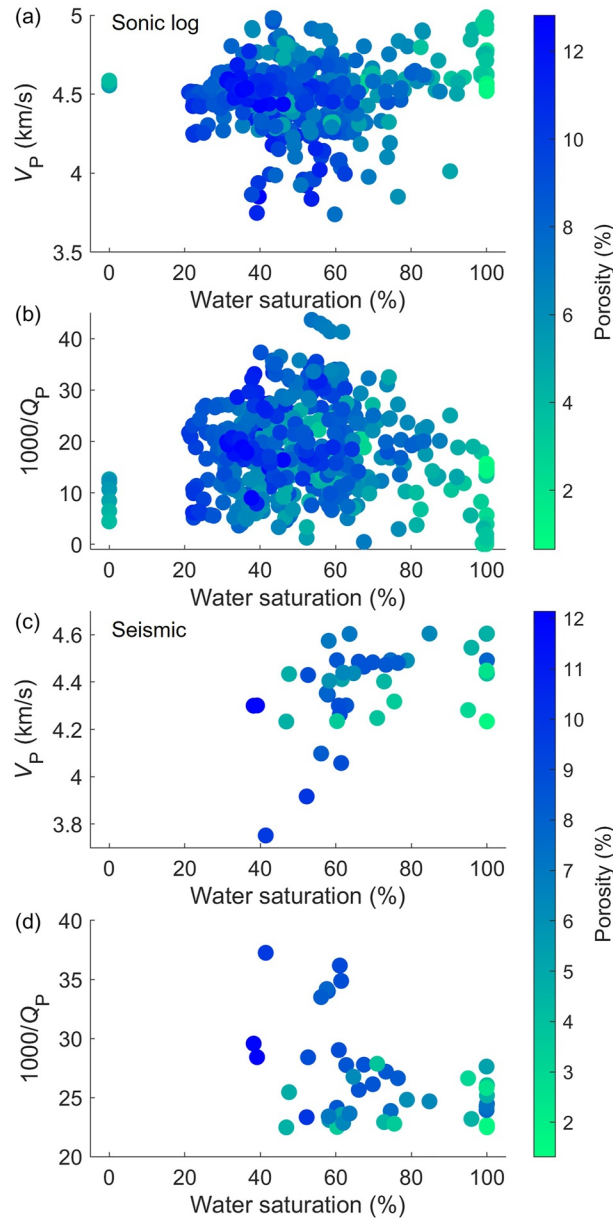


Figure 10. P-wave velocity and attenuation as a function of water saturation and porosity. (a, b) Correspond to sonic log data while (c, d) to seismic data.

where K_s is the grain bulk modulus, and K_b and μ_b are the bulk and shear moduli of the skeleton, respectively. The dilatation ratio β of the fluid bulk strain between the host with fluid 1 and inclusion (Ba et al., 2011) is

$$\beta = \frac{\phi_I}{\phi_H} \left[\frac{1 - (1 - \phi_H)K_s/K_H}{1 - (1 - \phi_I)K_s/K_I} \right] \quad (7)$$

where K_H and K_I are the bulk moduli of the host skeleton and inclusion, respectively. The dilatation ratio is 1 at the fluid boundary between fluid 1 and fluid 2 within the host.

According to Ba et al. (2017), the kinetic energy of the considered medium, where the fabric structure of two pore phases (stiff intergranular pores and soft pores/cracks) is presented in the solid skeleton, while at the same time the main skeleton with stiff pores are patchy-saturated, can be derived, for the case when the effect of WIFF is not incorporated.

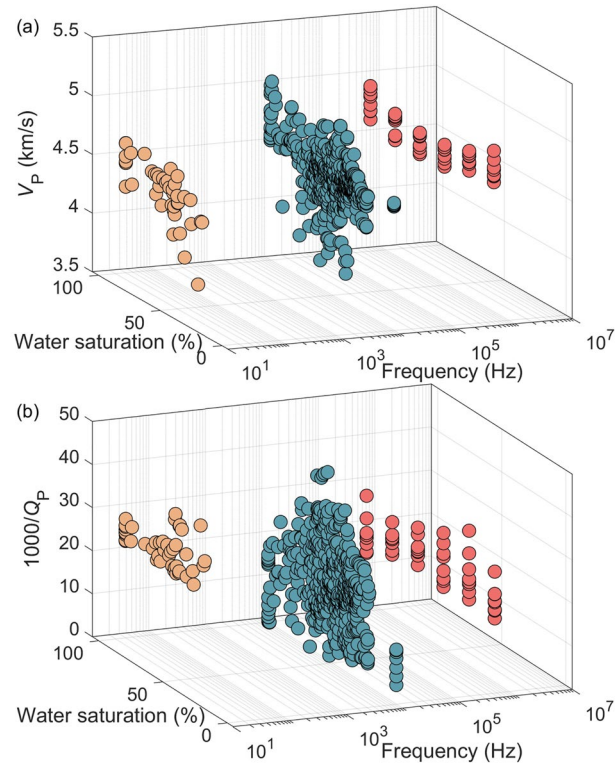


Figure 11. P-wave velocity (a) and attenuation (b) for the ultrasonic (red), sonic log (blue) and seismic (yellow) data sets as a function of frequency and water saturation.

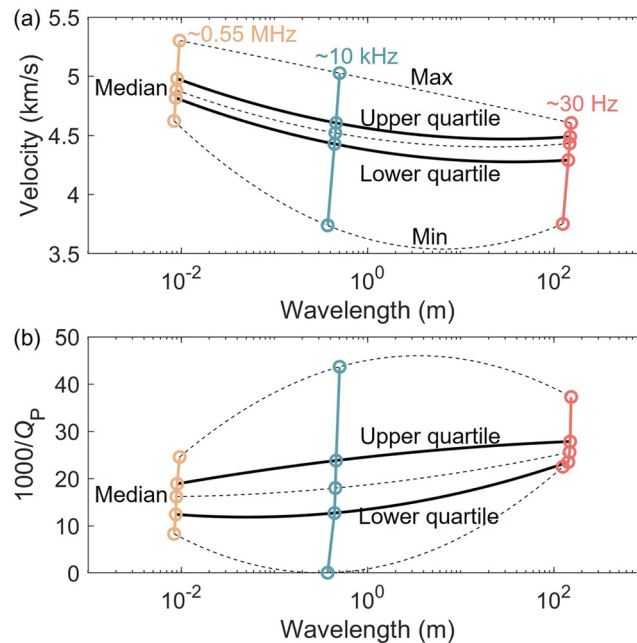


Figure 12. P-wave velocity (a) and attenuation (b) for the ultrasonic, sonic and seismic data sets as a function of wavelength. The maximum, quartiles, median and minimum are given by statistical analysis.

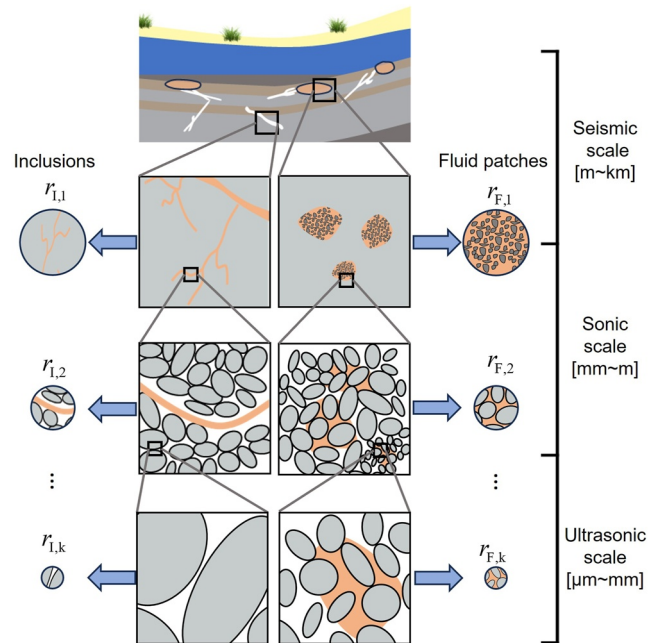


Figure 13. Inclusions with compliant pores and fluid patches in porous rocks at various scales. The radii of the inclusions and fluid patches follow a self-similarity distribution.

$$2T = \tilde{\rho}_{00} \sum_i \dot{u}_i^2 + 2 \sum_n \tilde{\rho}_{0n} \sum_i \dot{u}_i \dot{U}_i^{(n)} + \sum_n \tilde{\rho}_{nn} \sum_i (\dot{U}_i^{(n)})^2 \quad (8)$$

where $n = 1, 2$, and 3 correspond to the triple porosities of the host saturated with fluid 1, the inclusions saturated with fluid 1, and the host saturated with fluid 2, respectively, and u_i and U_i ($i = 1, 2$, and 3) are the solid and fluid displacement components, respectively.

The analytical relation between the radius of the spherical inclusions and the fluid increment can be derived for the kinetic energy associated with the WIFF process. The interactions between inclusions are neglected by assuming a sparse distribution of inclusions. The kinetic energy can be derived on the basis of the Biot-Rayleigh model (Ba et al., 2011) as

$$2T = \tilde{\rho}_{00} \sum_i \dot{u}_i^2 + 2 \sum_n \tilde{\rho}_{0n} \sum_i \dot{u}_i \dot{U}_i^{(n)} + \sum_n \tilde{\rho}_{nn} \sum_i (\dot{U}_i^{(n)})^2 + \frac{1}{3} \rho_{f1} \zeta_{H11}^2 r_I^3 \frac{[(1 - v_I)\phi_H]^2 \phi_I^2 d v_I}{\phi_H} + \frac{1}{3} \rho_{f1} \zeta_{H1H2}^2 r_F^3 [(1 - v_I)\phi_H]^3 S_{f1}^2 d S_{f2} \quad (9)$$

The density coefficients are

$$\begin{aligned} \tilde{\rho}_{11} &= \alpha_H \rho_{f1} (1 - v_I) \phi_H S_{f1}, \\ \tilde{\rho}_{22} &= \alpha_I \rho_{f1} \phi_I d v_I, \\ \tilde{\rho}_{33} &= \alpha_H \rho_{f2} (1 - v_I) \phi_H d S_{f2}, \\ \tilde{\rho}_{01} &= \rho_{f1} (1 - v_I) \phi_H S_{f1} - \tilde{\rho}_{11}, \\ \tilde{\rho}_{02} &= \rho_{f1} \phi_I d v_I - \tilde{\rho}_{22}, \\ \tilde{\rho}_{03} &= \rho_{f2} (1 - v_I) \phi_H d S_{f2} - \tilde{\rho}_{33}, \\ \tilde{\rho}_{00} &= (1 - \phi - d \phi_I - d \phi_{Hf2}) \rho_s - \tilde{\rho}_{01} - \tilde{\rho}_{02} - \tilde{\rho}_{03}, \end{aligned} \quad (10)$$

Table 2
Rock and Fluid Properties

Rock	Fluids		
ϕ	10.74%	K_{fw} (water)	2.5 GPa
K_s	38 GPa	η_{fw}	1 mPa · s
μ_s	44 GPa	ρ_{fw}	1.04 g/cm ³
K_b	11.8 GPa	K_{fg} (gas)	0.05 GPa
μ_b	13.9 GPa	η_{fg}	0.015 mPa · s
K_H	17.1 GPa	ρ_{fg}	0.117 g/cm ³
K_I	1.2 GPa	K_{fo} (oil)	1.27 GPa
ρ_s	2.65 g/cm ³	η_{fo}	5 mPa · s
v_I	3.70%	ρ_{fo}	0.79 g/cm ³
ϕ_H	10%		
ϕ_I	30%		
κ_H	0.01 D		
κ_I	1 D		

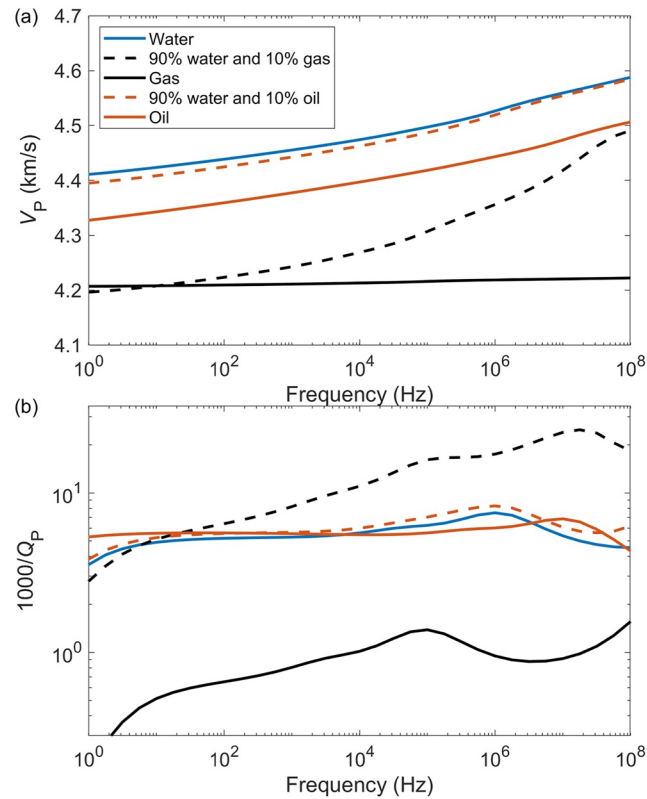


Figure 14. Theoretical P-wave velocity and attenuation in rocks saturated with different fluids. The fractal dimension is 2.6 and the radii range from 0.01 to 100 mm for the inclusions and fluid patches.

where ρ_s is the grain density, and α_H and α_I are the tortuosities of the host and inclusions, respectively.

The Biot dissipation accounting for the friction effects between the skeleton and pore fluids in the system is

$$2D = \sum_n \tilde{b}_n (\mathbf{u} - \mathbf{U}^{(n)}) \cdot (\mathbf{u} - \mathbf{U}^{(n)}) \quad (11)$$

where b_n is the Biot dissipation coefficient, \mathbf{u} and \mathbf{U} are the solid- and fluid-displacement vectors, respectively.

By considering the Biot loss and the dissipations induced by the two WIFFs, the dissipation function (Ba et al., 2017) is

$$2D = \tilde{b}_1 (\mathbf{u} - \mathbf{U}^{(1)}) \cdot (\mathbf{u} - \mathbf{U}^{(1)}) + \tilde{b}_2 (\mathbf{u} - \mathbf{U}^{(2)}) \cdot (\mathbf{u} - \mathbf{U}^{(2)}) + \tilde{b}_3 (\mathbf{u} - \mathbf{U}^{(3)}) \cdot (\mathbf{u} - \mathbf{U}^{(3)}) + \frac{1}{3} \eta_{f1} \zeta_{H1I1}^2 r_I^2 \frac{[(1 - v_I) \phi_H]^2 \phi_I^2 d v_I}{\tilde{\kappa}_H} + \frac{1}{3} \phi_H \eta_{f1} \zeta_{H1H2}^2 r_F^2 [(1 - v_I) \phi_H]^3 S_{f1}^2 d S_{f2} / \tilde{\kappa}_H \quad (12)$$

where $\tilde{\kappa}_H$ is the host permeability.

In accordance with Hamilton's principle, the Lagrangian density of the system is given by the equation $L = T - W$. The governing equations of wave propagation are derived by substituting the kinetic energy, potential energy and dissipation functions into the Lagrange equation, namely

$$\begin{aligned} \tilde{N} \nabla^2 \mathbf{u} + (\tilde{A} + \tilde{N}) \nabla e + \tilde{Q}_1 \nabla [\xi_{H1} + \zeta_{H1I1} \phi_I d v_I + \zeta_{H1H2} (1 - v_I) \phi_H d S_{f2}] \\ + \tilde{Q}_2 \nabla [\xi_{I1} - (1 - v_I) \phi_H \zeta_{H1I1}] + \tilde{Q}_3 \nabla [\xi_{H2} - (1 - v_I) \phi_H S_{f1} \zeta_{H1H2}] \\ = \tilde{\rho}_{00} \ddot{\mathbf{u}} + \tilde{\rho}_{01} \dot{\mathbf{U}}^{(1)} + \tilde{\rho}_{02} \dot{\mathbf{U}}^{(2)} + \tilde{\rho}_{03} \dot{\mathbf{U}}^{(3)} \\ + \tilde{b}_1 (\dot{\mathbf{u}} - \dot{\mathbf{U}}^{(1)}) + \tilde{b}_2 (\dot{\mathbf{u}} - \dot{\mathbf{U}}^{(2)}) + \tilde{b}_3 (\dot{\mathbf{u}} - \dot{\mathbf{U}}^{(3)}) \end{aligned} \quad (13a)$$

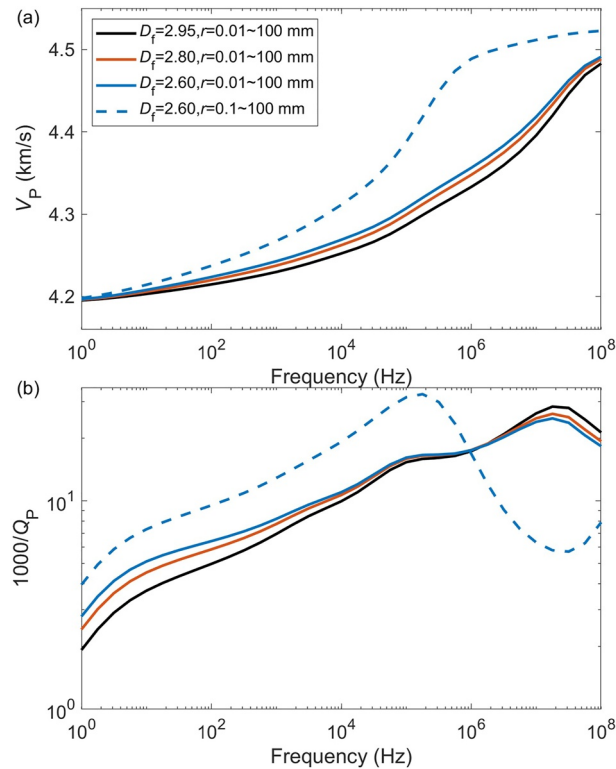


Figure 15. Theoretical P-wave velocity and attenuation with different fractal dimensions (D_f) and radius ranges (r) at gas-water saturation. The gas saturation is 10%.

$$\tilde{Q}_1 \nabla e + \tilde{R}_1 \nabla [\xi_{H1} + \zeta_{H111} \phi_I d v_I + \zeta_{H1H2} (1 - v_I) \phi_H d S_{f2}] = \tilde{\rho}_{01} \dot{\mathbf{u}} + \tilde{\rho}_{11} \ddot{\mathbf{U}}^{(1)} - \tilde{b}_1 (\dot{\mathbf{u}} - \dot{\mathbf{U}}^{(1)}) \quad (13b)$$

$$\tilde{Q}_2 \nabla e + \tilde{R}_2 \nabla [\xi_{I1} - (1 - v_I) \phi_H S_{f1} \zeta_{H111}] = \tilde{\rho}_{02} \dot{\mathbf{u}} + \tilde{\rho}_{22} \ddot{\mathbf{U}}^{(2)} - \tilde{b}_2 (\dot{\mathbf{u}} - \dot{\mathbf{U}}^{(2)}) \quad (13c)$$

$$\tilde{Q}_3 \nabla e + \tilde{R}_3 \nabla [\xi_{H2} - (1 - v_I) \phi_H \zeta_{H1H2}] = \tilde{\rho}_{03} \dot{\mathbf{u}} + \tilde{\rho}_{33} \ddot{\mathbf{U}}^{(3)} - \tilde{b}_3 (\dot{\mathbf{u}} - \dot{\mathbf{U}}^{(3)}) \quad (13d)$$

$$\begin{aligned} \phi_I [\tilde{Q}_1 e + \tilde{R}_1 (\xi_{H1} + \zeta_{H111} \phi_I d v_I)] d v_I - (1 - v_I) \phi_H [\tilde{Q}_2 e + \tilde{R}_2 (\xi_{I1} - (1 - v_I) \phi_H \zeta_{H111})] \\ = \frac{1}{3} r_I^2 [(1 - v_I) \phi_H]^2 \phi_I^2 d v_I \left(\frac{\rho_{f1}}{\phi_H} \ddot{\zeta}_{H111} + \frac{\eta_{f1}}{\kappa_H} \dot{\zeta}_{H111} \right) \end{aligned} \quad (13e)$$

$$\begin{aligned} [\tilde{Q}_1 e + \tilde{R}_1 (\xi_{H1} + \zeta_{H111} (1 - v_I) \phi_H d S_{f2})] (1 - v_I) \phi_H d S_{f2} \\ - (1 - v_I) \phi_H S_{f1} [\tilde{Q}_3 e + \tilde{R}_3 (\xi_{I1} - (1 - v_I) \phi_H S_{f1} \zeta_{H1H2})] \\ = \frac{1}{3} r_F^2 ((1 - v_I) \phi_H)^3 S_{f1}^2 d S_{f2} \left(\frac{\rho_{f1}}{(1 - v_I) \phi_H} \ddot{\zeta}_{H1H2} + \frac{\eta_{f1}}{\kappa_H} \dot{\zeta}_{H111} \right) \end{aligned} \quad (13f)$$

where e is the solid divergence field. The complex wave numbers are computed by the plane-wave analysis method, and we obtain the complex moduli of the composite media. After each addition of inclusions, the composite media can be treated as a dissipative homogeneous porous medium containing an equivalent fluid. The fluid bulk modulus can then be computed using the Gassmann equation (Gassmann, 1951), which takes into account the fluid properties in the host at the next addition.

At each addition, the size of the inclusions and fluid patches follow the correlation function $d\phi_I = \phi_I'(r_I) dr_I$ and $dS_{f2} = S_{f2}'(r_F) dr_F$ (Klimeš, 2002), respectively. Then, the wave propagation equations of the proposed model are

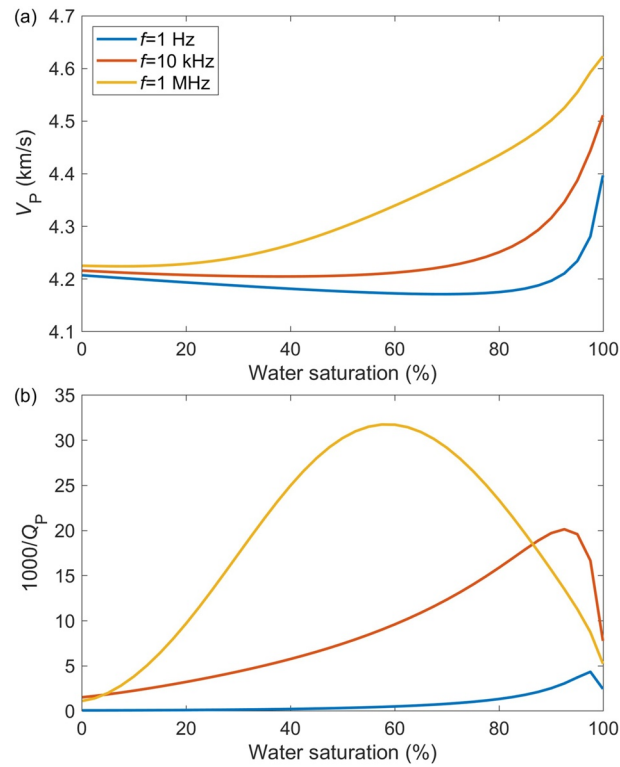


Figure 16. Theoretical P-wave velocity and attenuation as a function of water saturation at 1 Hz, 10 kHz and 1 MHz in the gas-water saturated case. The fractal dimension is 2.6 and the radius range is 0.1–100 mm for the inclusions and fluid patches.

$$\begin{aligned} & \bar{N}\nabla^2\mathbf{u} + (\bar{A} + \bar{N})\nabla e + \bar{Q}_1\nabla\left[\xi_{H1} + \int_0^\infty \zeta_{H1I1}\phi'_I(r_I)dr_I + \int_0^\infty \zeta_{H1H2}(1-v_I)\phi_H S'_{f2}(r_F)dr_F\right] \\ & + \int_0^\infty \bar{Q}_2\phi'_I(r_I)\nabla[\xi_{I1} - \phi_I\zeta_{H1I1}]dr_I + \int_0^\infty \bar{Q}_3(1-v_I)\phi_H S'_{f2}(r_F)\nabla[\xi_{H2} - (1-v_I)\phi_H S_{f2}\zeta_{H1H2}]dr_F \quad (14a) \\ & = \bar{\rho}_{00}\ddot{\mathbf{u}} + \bar{\rho}_{01}\dot{\mathbf{U}}^{(1)} + \bar{\rho}_{02}\dot{\mathbf{U}}^{(2)} + \bar{\rho}_{03}\dot{\mathbf{U}}^{(3)} + \bar{b}_1(\dot{\mathbf{u}} - \dot{\mathbf{U}}^{(1)}) + \bar{b}_2(\dot{\mathbf{u}} - \dot{\mathbf{U}}^{(2)}) + \bar{b}_3(\dot{\mathbf{u}} - \dot{\mathbf{U}}^{(3)}) \end{aligned}$$

$$\begin{aligned} & \bar{Q}_1\nabla e + \bar{R}_1\nabla\left[\xi_{H1} + \int_0^\infty \zeta_{H1I1}\phi'_I(r_I)dr_I + \int_0^\infty \zeta_{H1H2}(1-v_I)\phi_H S'_{f2}(r_F)dr_F\right] \\ & = \bar{\rho}_{01}\ddot{\mathbf{u}} + \bar{\rho}_{11}\dot{\mathbf{U}}^{(1)} - \bar{b}_1(\dot{\mathbf{u}} - \dot{\mathbf{U}}^{(1)}) \quad (14b) \end{aligned}$$

$$\bar{Q}_2\nabla e + \bar{R}_2\nabla[\xi_{I1} - \phi_I v_I \zeta_{H1I1}] = \bar{\rho}_{02}\ddot{\mathbf{u}} + \bar{\rho}_{22}\dot{\mathbf{U}}^{(2)} - \bar{b}_2(\dot{\mathbf{u}} - \dot{\mathbf{U}}^{(2)}) \quad (14c)$$

$$\bar{Q}_3\nabla e + \bar{R}_3\nabla[\xi_{H2} - (1-v_I)\phi_H S_{f2}\zeta_{H1H2}] = \bar{\rho}_{03}\ddot{\mathbf{u}} + \bar{\rho}_{33}\dot{\mathbf{U}}^{(3)} - \bar{b}_3(\dot{\mathbf{u}} - \dot{\mathbf{U}}^{(3)}) \quad (14d)$$

$$\begin{aligned} & \left[\bar{Q}_1 e + \bar{R}_1\left(\xi_{H1} + \int_0^\infty \zeta_{H1I1}\phi'_I(r_I)dr_I\right)\right] - \left[\bar{Q}_2 e + \bar{R}_2(\xi_{I1} - (1-v_I)\phi_H \zeta_{H1I1})\right] \\ & = \frac{1}{3}r_I^2(1-v_I)\phi_H\phi_I\left(\frac{\rho_{f1}}{\phi_H}\ddot{\zeta}_{H1I1}^2 + \frac{\eta_{f1}}{\kappa_H}\dot{\zeta}_{H1I1}\right) \quad (14e) \end{aligned}$$

$$\begin{aligned} & \bar{Q}_1 e + \bar{R}_1\left(\xi_{H1} + \int_0^\infty \zeta_{H1H2}(1-v_I)\phi_H S'_{f2}(r_F)dr_F\right) - \left[\bar{Q}_3 e + \bar{R}_3(\xi_{H2} - (1-v_I)\phi_H S_{f2}\zeta_{H1H2})\right] \\ & = \frac{1}{3}r_F^2((1-v_I)\phi_H)^2 S_{f2}\left(\frac{\rho_{f1}}{(1-v_I)\phi_H}\ddot{\zeta}_{H1H2}^2 + \frac{\eta_{f1}}{\kappa_H}\dot{\zeta}_{H1H2}\right) \quad (14f) \end{aligned}$$

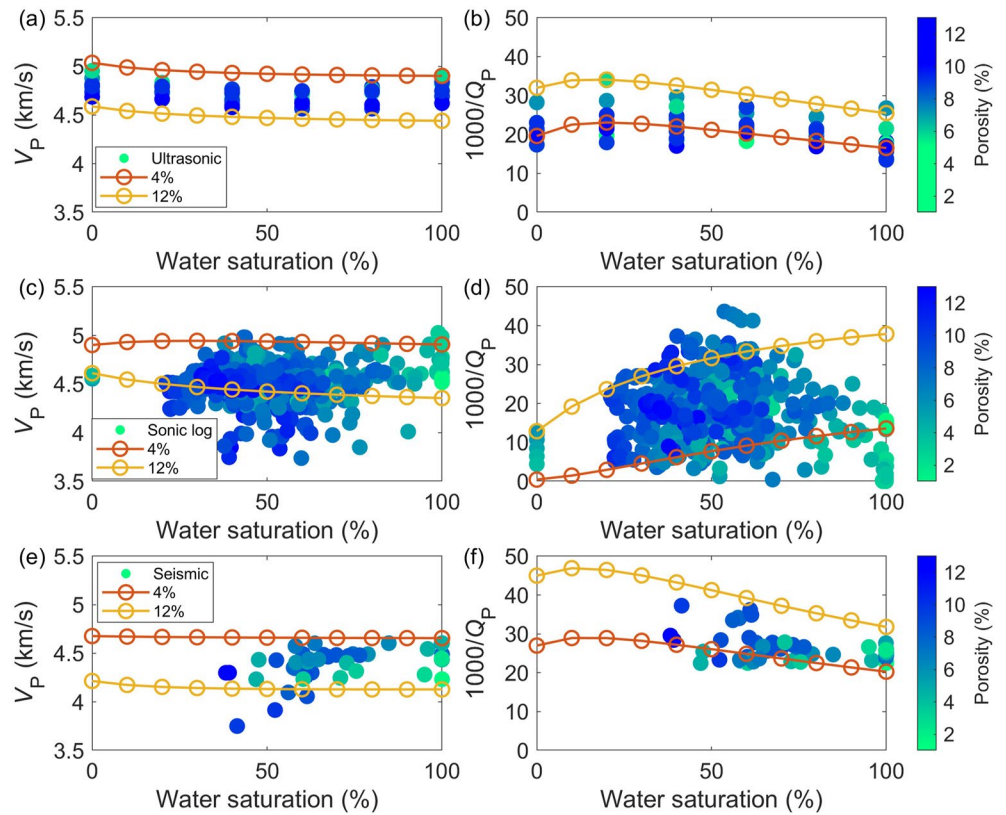


Figure 17. Comparisons between the theoretical results at 4% and 12% porosities and the measured data sets at different saturations and porosities. (a, b) 0.55 MHz, (c, d) 10 kHz, and (e, f) 30 Hz.

where the stiffnesses \bar{A} , \bar{N} , \bar{Q}_1 , \bar{Q}_2 , \bar{Q}_3 , \bar{R}_1 , \bar{R}_2 , and \bar{R}_3 , and the density coefficients $\bar{\rho}_{00}$, $\bar{\rho}_{01}$, $\bar{\rho}_{02}$, $\bar{\rho}_{03}$, $\bar{\rho}_{11}$, $\bar{\rho}_{22}$, and $\bar{\rho}_{33}$ can be obtained based on the above discretization procedures of Equations 5–14. P-wave velocity and attenuation can be computed with the P-wave numbers (k) at the final iteration, as

$$V_P = \frac{\omega}{\text{Re}(k)} \quad (15)$$

$$Q_P^{-1} = \frac{2\text{Im}(k)}{\text{Re}(k)} \quad (16)$$

where ω is angular frequency.

The frequency- and saturation-dependent seismic wave responses of the fractal partially-saturated media are analyzed with this model. The rock properties in the numerical modeling are based on the parameters of Ba et al. (2011) and Pride and Berryman (2003), as are shown in Table 2. The radius distributions of the inclusions and fluid patches satisfy the self-similarity features. The volume fractions are related to the scale ranges of the inclusions and fluid patches as $v = 1 - (r_{\min}/r_{\max})^{3-D_f}$, where D_f is the fractal dimension while r_{\min} and r_{\max} are the minimum and maximum radii of the inclusions and fluid patches, respectively. The inclusions and fluid patches have identical values for both fractal dimension and radius range, with the former at 2.6 and the latter between 0.01 and 100 mm. Figure 14 shows the frequency-dependent velocity and attenuation in porous rocks saturated with different fluids. When the rock is saturated with a fluid, the attenuation is associated with the WIFF between stiff and compliant pores. When the rock is partially saturated with gas and water, a strong attenuation peak occurs in a higher frequency range due to the WIFF between the interfaces of the two fluid types. The WIFF at oil-water interfaces is weaker due to the similar fluid properties.

Figure 15 illustrates the velocity and attenuation as a function of frequency under partial gas-water saturation for different fractal dimensions and radius ranges. The fractal dimension and radius range of the inclusions and fluid

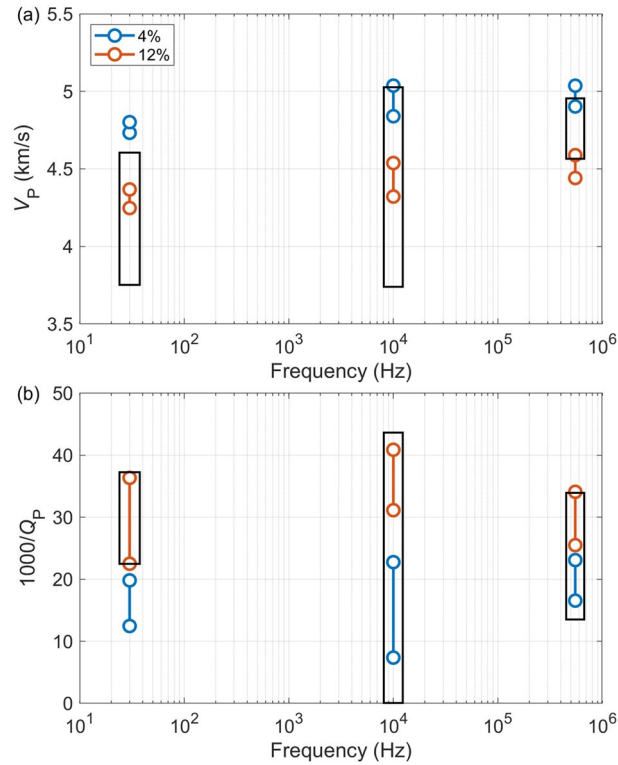


Figure 18. Comparison between the theoretical model results at different saturations for 4% and 12% porosities (circles with bar), and the measured data sets falling within each rectangular box at the observed frequencies.

patches are the same. When the radius range is constant, the velocity decreases slightly with increasing fractal dimension, while the loss shows similar behavior. The inflection point of velocity dispersion and loss peak caused by the two WIFF mechanisms shift to lower frequencies as the radius minimum increases.

Figure 16 shows the P-wave velocity and attenuation as a function of water saturation for a fractal dimension of 0.1–100 mm. At ultrasonic, sonic and seismic frequencies, the P-wave velocity initially decreases and then increases rapidly with increasing water saturation. This is due to the comparable or greater effect of the equivalent density of gas and water mixtures on velocity compared to the equivalent P-wave modulus in the presence of water. A similar relationship between velocity and saturation is observed in Batzle et al. (2006). The attenuation peak shifts toward lower water saturation with increasing frequency. The proposed model is able to describe the strong velocity dispersion in saturated rocks, whereas most previous partial-saturation models, which only consider heterogeneities caused by fluid distribution, give similar velocity predictions at the full saturation for the seismic and ultrasonic frequencies (e.g., Müller et al., 2008).

Table 3
Rock and Fluid Properties of Sample Fon3 (Zhao et al., 2021)

Rock	Fluids
ϕ	6.40%
K_s	37 GPa
μ_s	44 GPa
K_b	5.0 GPa
μ_b	6.2 GPa
K_H	11.5 GPa
K_I	0.035 GPa
ρ_s	2.64 g/cm ³
v_I	2%
ϕ_H	6.12%
ϕ_I	15%
κ_H	0.024 D
κ_I	0.24 D

5. Modeling and Analysis

Modeling is performed to understand the wave responses of the considered tight reservoirs at different saturations and frequencies. The bulk modulus of the grain is 38.78 GPa, calculated by using the measured mineral compositions based on the Hashin-Shtrikman limits (Hashin & Shtrikman, 1963). The average density is 2.65 g/cm³. The bulk moduli of the host skeleton are 26 and 20 GPa, while the shear moduli are 23 and 18 GPa for porosities of 4% and 12%, respectively. The permeabilities are 0.0068 and 0.2377 mD with the corresponding porosities based on the measured pore-permeability relation-

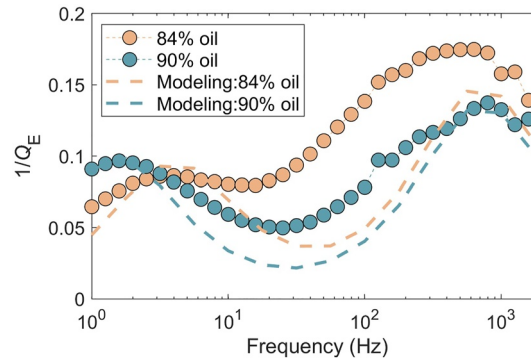


Figure 19. Comparison between the theoretical and measured extensional attenuation at different oil saturations.

ship. The content, bulk modulus, and shear modulus of the inclusions with 25% porosity are 0.04, 0.75 GPa, and 0.61 GPa, respectively, while their permeabilities are an order of magnitude larger than those of the host material due to the compliant pores with good connectivity. The bulk modulus, density, and viscosity of water and oil are 2.273 and 1.99 GPa, 1.004 and 0.89 g/cm³, and 0.981 and 8 mPa · s, respectively, under in situ conditions according to the formula of Batzle and Wang (Batzle & Wang, 1992). The fractal dimension of the inclusions with cracks is determined to be 2.67 and 2.45 at 4% and 12% porosity, respectively, based on the pore structure analysis in Figure 3, while the radius range is adjusted to match the observed multiscale data sets. The fractal dimension of the fluid patches is the same as that of the inclusions, while their size is adjusted based on the measured data. Figure 17 compares the model results with the ultrasonic, sonic log, and seismic data at different porosities and water saturations. Figures 17a and 17b show the velocity and attenuation at the ultrasonic frequency. The radii of the inclusions and fluid patches are set to 0.32–25.1 μm and 0.1–4 μm at 12% and 4% porosities, respectively. The results show that the velocity decreases with water saturation, while the attenuation, consistent with the measured results, is stronger at high oil saturation. The inclusions and fluid patches are larger in samples with a higher porosity, which affects the ultrasonic loss. Figures 17c–17f show the sonic and seismic data, respectively. The bulk and shear moduli of the host skeleton are 24–21 GPa and 18–16 GPa for 4% and 12% porosities, respectively, due to the presence of larger heterogeneities. In contrast, the bulk and shear moduli of the inclusions with larger cracks change to 0.35 and 0.24 GPa, respectively. The radii of the inclusions and fluid patches are set to 0.32 μm to 2.8 mm at 12% porosity, which corresponds to 0.32 μm to 0.25 mm at sonic frequencies, and 1 μm to 2.8 mm at seismic frequencies. The radius ranges from 0.1 μm to 0.06 mm at sonic frequencies and 0.1 μm to 0.5 mm at seismic frequencies for 4% porosity. Similar velocity-saturation relationships are observed in the measured frequencies, while the attenuation-saturation relationships are different between the different frequency ranges. Discrepancies between the model results and observed data are attributed to a variety of factors, including the uncertainty in input parameters, the presence of minor gas, and the scattering effect. The parameters used for modeling are determined with experimental measurements, that may not fully reflect the in-situ reservoir properties. Figure 18 presents the ranges of model results with different saturations for 4% and 12% porosities compared to the ranges of measured data at the observed frequencies. The model results generally fall within the boxes representing the measurement data sets and are consistent with the trend of measured P-wave velocities and attenuation with respect to frequency. The proposed model well describes the wave responses across a broadband frequency range of tight oil reservoirs.

The extensional attenuation data ($1/Q_E$) of a partially air-oil saturated Fontainebleau sandstone sample Fon3 is obtained between 1 and 2,000 Hz by using the stress-strain oscillation experiments by Zhao et al. (2021). The sample, 37.9 mm in diameter and 51.4 mm in length, is approximately 99.9% quartz and has a porosity of 6.40%, a permeability of 24 mD, and a density of 2.472 g/cm³. A micro-CT image and scanning electron microscope micrograph show numerous grain contacts and narrow microcracks. The sample is saturated by using the pseudo-imbibition saturation method, resulting in an oil saturation of ~90%. Oil saturation is then changed to ~84% by pumping air into the sample. Low frequency experiments are performed at both saturation states. The rock properties are listed in Table 3. The fractal dimension of the inclusion and air patch is 2.45, while their size ranges are considered as fitting parameters. Figure 19 compares the modeling results with the measured data and shows the agreement. The theoretical extensional attenuation is estimated based on the equation $(1 + \nu)/$

$Q_E = (1 - \nu)(1 - 2\nu)/Q_p + 2\nu(2 - \nu)/Q_s$ (Winkler & Nur, 1979), where $1/Q_s$ is the S-wave attenuation and ν is the Poisson ratio. The crack radii range from 0.16 to 7.9 mm. The radii of the fluid patches are 5–20 mm and 4–15.8 mm when the oil saturation is 84% and 90%, respectively. The damping peaks at the lower frequencies are attributed to the WIFF at the air-oil interfaces, while the peaks at the higher frequencies are attributed to the WIFF between compliant cracks and stiff pores. The damping peaks observed in the data are interpreted by Zhao et al. (2021) to be caused by mesoscopic flow from air patches with a radius of 11 mm, as well as by microcrack-induced squirt flow. The discrepancy between the observed and predicted attenuation at relatively high frequencies can be attributed to the vibration of the oil-gas interfaces. Furthermore, only the Biot global flow is considered for S-wave attenuation estimation in our model, leading to a smaller theoretical value.

6. Discussions

6.1. Saturation Effect on Different Rock Types

The effects of saturation and frequency on tight rocks may vary due to differences in lithology and saturation methods, independent of measurement setups and conditions. The relations between rock responses and saturation and the discrepancies between different measurement methods in tight rocks are analyzed. The P-wave velocity-saturation ($V_p - S_w$) relationship measured in this study, which shows that velocity decreases first and increases with water saturation, differs from those reported in literature. Some measurements indicate that V_p increases with S_w at oil-water saturation tests (e.g., Ba et al., 2017; El-Husseiny et al., 2019) while other studies show that V_p at oil or partially oil-saturated conditions is larger than that saturated with water (e.g., Pei et al., 2011; Xie et al., 2022). In our measurements, V_p decreases until S_w reaches 40% or 60%. Clay minerals may swell when interacting with water, resulting in softening of the rock skeleton. The rock may also be stiffened by the coupling effect between oil and rock skeleton due to the higher oil viscosity. Moreover, the fluid distribution may change when oil is injected into water-saturated rocks, resulting in a variation of the $V_p - S_w$ trend. Further study of the effects of saturation history is needed to improve understanding of the oil accumulation characteristics of tight reservoirs.

Various wave-induced flow mechanisms can occur at different observation scales, including local fluid flow at the pore and mesoscopic scales and WIFF caused by the inhomogeneous distribution of pore fluid at the mesoscopic and macroscopic scales, leading to wave dispersion/attenuation. In our study, the loss variation is affected by the crack size and properties, and fluid saturation and distribution. If the saturation changes slightly, the larger loss variation may be due to the pore fluid distribution changing significantly from heterogeneous patches to a homogeneous distribution on the pore scale. Microscopic squirt flow has also been considered as a mechanism leading to the measured velocity dispersion (e.g., Mikhailsevitch et al., 2016; Spencer & Shine, 2016). In a porous rock, fluid can flow from a compliant microcrack to a less compliant neighboring pore depending on the shape and size of the inclusions (O'Connell & Budiansky, 1977). In addition, the scattering effect and other dissipation mechanisms that may affect wave propagation, such as intergranular friction, and slip at the interface in the tangential direction between the inclusions and the host, are not considered (He et al., 2022; Winkler et al., 1979). The proposed model can be extended by including these factors. The rock physical parameters used in modeling could be more accurately determined by accounting for the significant differences in measured porosity and permeability caused by spatial heterogeneity and scaling (J. Li et al., 2020; Mukhametdinova et al., 2020). The model assumes spherical inclusions, which is a simplification of the actual geometry of fluid patches and fractures in reservoirs. The geometric characteristics of heterogeneities are more complex than the simple approximation, which may affect the attenuation behaviors.

6.2. Implications on Tight Reservoirs

Interpretation of multiscale data, from core plug to seismic, must take into account the various scales of heterogeneities with geologic and physical significance. A unique correlation resulting from a theory of multiscale wave propagation can constrain the seismic profile with logging and core data, improving the accuracy of the inversion (e.g., Batzle et al., 2006; Borgomano et al., 2019). To address the problem of scaling in seismic exploration, Partyka et al. (2000) established a correspondence between seismic data and experimental observations using the Backus average and demonstrated the validity of the approach. Dvorkin and Wollner (2017) hypothesized that a rock-physics transformation can be scale-independent. This is confirmed by the consistency between the

velocity-porosity relationship determined from cores and that inferred by the resulting rock-physics transform from log data in carbonates (El-Husseiny et al., 2019). However, our observations differ from this case due to the complex relationships between velocity/attenuation and porosity/saturation, which are primarily determined by various factors (e.g., cracks or fluid distribution) at different scales. Core properties are controlled by microstructures and fluid and exhibit marked heterogeneity due to diagenetic processes. Reservoir properties are also affected by large-scale structural features. This discrepancy arises because the core plug does not substantially exhibit large-scale heterogeneities. Tight oil reservoir modeling shows that various heterogeneities, including pores, fractures, and fluid patches, must be considered when upscaling elastic properties and attenuation.

Rock and fluid properties can be predicted based on the proposed model and seismic data if the relationships obtained from well logs and seismic data sets are representative of the tight reservoirs (e.g., Luo et al., 2023). Variations in wave velocity and attenuation with saturation may be indicative of pore geometry and fluid distribution. Velocity decreases while attenuation increases with crack content. Rock samples with higher crack contents are expected to be more sensitive to saturation changes. The measured experimental data show that the velocity variation is less than 6% with saturation, while the attenuation variation averages 23.75%. The relationship between attenuation and saturation does not follow a monotonic trend, resulting in the saturation inversion being non-unique. The changes in seismic properties at different saturations can be represented by combining elastic properties and attenuation (i.e., attenuation divided by velocity), which provides a better indication of oil and gas. In addition, studies have shown that structural heterogeneity, characterized by pore scale and spatial distribution, can influence oil recovery during waterflooding (e.g., Al-Shalabi & Ghosh, 2016; Y. Xu et al., 2017). For rocks with high porosity, water is displaced more quickly and easily in connected pores than in isolated or microscale pores with lower permeabilities, leaving a large amount of water behind and resulting in high water saturation. Conversely, rocks with a more homogeneous pore structure, consisting mainly of intergranular pores, may exhibit more homogeneous displacement of fluids. This could correspond to the expected changes in seismic signature caused in practice by oil production or flooding with water for enhanced oil recovery, which can be described by the proposed fractal model.

The P-wave velocity and attenuation characteristics observed in this study, which vary with saturation and frequency, are specific to the tight-oil reservoirs of the Ordos Basin. Significant differences can occur in sandstone and carbonate reservoirs with higher fracture content or higher gas saturation (e.g., H. Li et al., 2020; Y. Wei et al., 2021). The presence of methane or CO₂ injections, which can significantly alter rock properties, can be investigated in another study. Future work could extend the frequency range of the experimental measurements, since only three data sets with different frequencies are currently available. Data from broadband experiments (e.g., Borgomano et al., 2019) and vertical seismic profiles (e.g., Sams et al., 1997) can be acquired so as to investigate the multiscale relationship at broader frequency ranges. In addition, multiscale observations can be used to create the training data sets and use a deep neural network to create a rock physics transform relationship, making it suitable for field applications.

7. Conclusions

Laboratory, well-log, and seismic data are collected from the Ordos Basin tight-oil reservoirs in China. Ultrasonic tests are performed on eight sandstone samples under in situ conditions, and the wave responses of the corresponding sandstone layers are determined. Intergranular pores, dissolution pores, and microcracks with a small amount of clay on the grain surfaces are observed in the cast thin sections of the samples. The pore diameters are mainly between 0.05 and 8 μm , and the fractal dimensions of the pores are between 2.45 and 2.67 at the reservoir porosity range. The probability density of cracks with aspect ratio less than 0.01 is about 0.03. A linear relationship is also observed between sample porosity and log of permeability.

P-wave velocities and attenuation are determined with the multiscale wavedata sets. Velocities decrease with porosity, while attenuation is stronger with partial saturation. Descriptive statistics of the three data sets show that the average velocity dispersion is 8.02% as the wavelength increases from ultrasonic to sonic measurements. In contrast, a dispersion of 2% is observed as the wavelength increases from the sonic to the seismic observation. The average attenuation increases with increasing wavelength from 16.13 to 25.56. A partial-saturation model that accounts for fractal inclusions and fluid stains is derived based on the differential effective medium theory and the double double-porosity model. Modeling results show that the fluid properties, saturation, and scale

range of heterogeneities significantly affect the wave responses. The relationship between attenuation and saturation depends on the measured frequencies. By matching the model results with the measured multiscale data, the radii of cracks and fluid patches are considered to range from 0.1 μm to 2.8 mm in tight-oil reservoirs. Based on the proposed model and seismic data, the reservoir and fluid properties can be inferred from the quantitative characteristics of rock physics.

Data Availability Statement

Experimental waveform data for this article can be found at <https://doi.org/10.5281/zenodo.8174303>. The measurements of a Fontainebleau sandstone sample can be found in Zhao et al. (2021) (<https://doi.org/10.1093/gji/ggaa551>).

Acknowledgments

This work was supported by the National Natural Science Foundation of China (Grant 41974123, 42174161, 41930431, and 42274173), the Natural Science Foundation of Heilongjiang Province of China (Grant YQ2023D005), and the Fundamental Research Funds for the Central Universities (Grant B210201032).

References

- Adam, L., Batzle, M. L., Lewallen, K. T., & Wijk, K. (2009). Seismic wave attenuation in carbonates. *Journal of Geophysical Research*, 114(B6), B06208. <https://doi.org/10.1029/2008JB005890>
- Aki, K., & Richards, P. (2002). *Quantitative seismology: Theory and methods* (2nd ed.). University Science Books.
- Akram, J., & Eaton, D. W. (2016). A review and appraisal of arrival-time picking methods for downhole microseismic data. *Geophysics*, 81(2), KS71–KS91. <https://doi.org/10.1190/geo2014-0500.1>
- Al-Shalabi, E. W., & Ghosh, B. (2016). Effect of pore-scale heterogeneity and capillary-viscous fingering on commingled waterflood oil recovery in stratified porous media. *Journal of Petroleum Engineering*, 2016, e1708929. <https://doi.org/10.1155/2016/1708929>
- Amalokwu, K., Best, A. I., Sothcott, J., Chapman, M., Minshull, T., & Li, X.-Y. (2014). Water saturation effects on elastic wave attenuation in porous rocks with aligned fractures. *Geophysical Journal International*, 197(2), 943–947. <https://doi.org/10.1093/gji/ggu076>
- Ba, J., Carcione, J. M., & Nie, J. X. (2011). Biot-Rayleigh theory of wave propagation in double-porosity media. *Journal of Geophysical Research*, 116(B6), B06202. <https://doi.org/10.1029/2010JB008185>
- Ba, J., Ma, R., Carcione, J. M., & Picotti, S. (2019). Ultrasonic wave attenuation dependence on saturation in tight oil siltstones. *Journal of Petroleum Science and Engineering*, 179, 1114–1122. <https://doi.org/10.1016/j.petrol.2019.04.099>
- Ba, J., Xu, W., Fu, L.-Y., Carcione, J. M., & Zhang, L. (2017). Rock anelasticity due to patchy saturation and fabric heterogeneity: A double double-porosity model of wave propagation. *Journal of Geophysical Research: Solid Earth*, 122(3), 1949–1976. <https://doi.org/10.1002/2016JB013882>
- Ba, J., Zhao, J., Carcione, J. M., & Huang, X. (2016). Compressional wave dispersion due to rock matrix stiffening by clay squirt flow: Clay squirt flow in tight siltstone. *Geophysical Research Letters*, 43(12), 6186–6195. <https://doi.org/10.1002/2016GL069312>
- Bailey, C., Fortin, J., Adelinet, M., & Hamon, Y. (2019). Upscaling of elastic properties in carbonates: A modeling approach based on a multiscale geophysical data set. *Journal of Geophysical Research: Solid Earth*, 124(12), 13021–13038. <https://doi.org/10.1029/2019JB018391>
- Batzle, M. L., Han, D.-H., & Hofmann, R. (2006). Fluid mobility and frequency-dependent seismic velocity — Direct measurements. *Geophysics*, 71(1), N1–N9. <https://doi.org/10.1190/1.2159053>
- Batzle, M. L., & Wang, Z. (1992). Seismic properties of pore fluids. *Geophysics*, 57(11), 1396–1408. <https://doi.org/10.1190/1.1443207>
- Best, A. I., & Sams, M. S. (1997). Compressional wave velocity and attenuation at ultrasonic and sonic frequencies in near-surface sedimentary rocks. *Geophysical Prospecting*, 45(2), 327–344. <https://doi.org/10.1046/j.1365-2478.1997.00337.x>
- Biot, M. A. (1956). Theory of propagation of elastic waves in a fluid-saturated porous solid. I. Low-frequency range. *Journal of the Acoustical Society of America*, 28(2), 168–178. <https://doi.org/10.1121/1.1908239>
- Borgomano, J. V. M., Pimienta, L. X., Fortin, J., & Guéguen, Y. (2019). Seismic dispersion and attenuation in fluid-saturated carbonate rocks: Effect of microstructure and pressure. *Journal of Geophysical Research: Solid Earth*, 124(12), 12498–12522. <https://doi.org/10.1029/2019JB018434>
- Cadoret, T., Mavko, G., & Zinszner, B. (1998). Fluid distribution effect on sonic attenuation in partially saturated limestones. *Geophysics*, 63(1), 154–160. <https://doi.org/10.1190/1.1444308>
- Carcione, J. M. (2022). *Wave fields in real media: Wave propagation in anisotropic, anelastic porous and electromagnetic media* (4th ed.). Elsevier Science.
- Carcione, J. M., Poletto, F., & Farina, B. (2018). The Burgers/squirt-flow seismic model of the crust and mantle. *Physics of the Earth and Planetary Interiors*, 274, 14–22. <https://doi.org/10.1016/j.pepi.2017.10.008>
- Carcione, J. M., Poletto, F., Farina, B., & Bellezza, C. (2018). 3D seismic modeling in geothermal reservoirs with a distribution of steam patch sizes, permeabilities and saturations, including ductility of the rock frame. *Physics of the Earth and Planetary Interiors*, 279, 67–78. <https://doi.org/10.1016/j.pepi.2018.03.004>
- Chapman, S., Borgomano, J. V. M., Quintal, B., Benson, S. M., & Fortin, J. (2021). Seismic wave attenuation and dispersion due to partial fluid saturation: Direct measurements and numerical simulations based on X-Ray CT. *Journal of Geophysical Research: Solid Earth*, 126(4), e2021JB021643. <https://doi.org/10.1029/2021JB021643>
- Chapman, S., Quintal, B., Tisato, N., & Holliger, K. (2017). Frequency scaling of seismic attenuation in rocks saturated with two fluid phases. *Geophysical Journal International*, 208(1), 221–225. <https://doi.org/10.1093/gji/ggw387>
- Chapman, S., Tisato, N., Quintal, B., & Holliger, K. (2016). Seismic attenuation in partially saturated Berea sandstone submitted to a range of confining pressures. *Journal of Geophysical Research: Solid Earth*, 121(3), 1664–1676. <https://doi.org/10.1002/2015JB012575>
- Chen, X., Zhong, W., He, Z., & Zou, W. (2016). Frequency-dependent attenuation of compressional wave and seismic effects in porous reservoirs saturated with multi-phase fluids. *Journal of Petroleum Science and Engineering*, 147, 371–380. <https://doi.org/10.1016/j.petrol.2016.08.031>
- Dvorkin, J., & Nur, A. (2009). Scale of experiment and rock physics trends. *The Leading Edge*, 28(1), 110–115. <https://doi.org/10.1190/1.3064155>
- Dvorkin, J., & Wollner, U. (2017). Rock-physics transforms and scale of investigation. *Geophysics*, 82(3), MR75–MR88. <https://doi.org/10.1190/geo2016-0422.1>
- El-Husseiny, A., Vega, S., & Nizamuddin, S. (2019). The effect of pore structure complexity and saturation history on the variations of acoustic velocity as function of brine and oil saturation in carbonates. *Journal of Petroleum Science and Engineering*, 179, 180–191. <https://doi.org/10.1016/j.petrol.2019.04.019>

- Feder, J. (1988). *Fractals*. Plenum Press.
- Fu, J., Li, S., Niu, X., Deng, X., & Zhou, X. (2020). Geological characteristics and exploration of shale oil in Chang 7 Member of Triassic Yanchang Formation, Ordos Basin, NW China. *Petroleum Exploration and Development*, 47(5), 931–945. [https://doi.org/10.1016/S1876-3804\(20\)60107-0](https://doi.org/10.1016/S1876-3804(20)60107-0)
- Gassmann, F. (1951). Über die elastizität poroser medien. *Vierteljahrsschrift der Naturforschenden Gesellschaft in Zürich*, 96, 1–23.
- Guo, J., & Gurevich, B. (2020). Frequency-dependent P wave anisotropy due to wave-induced fluid flow and elastic scattering in a fluid-saturated porous medium with aligned fractures. *Journal of Geophysical Research: Solid Earth*, 125(8), e2020JB020320. <https://doi.org/10.1029/2020JB020320>
- Gurevich, B., Makarynska, D., de Paula, O. B., & Pervukhina, M. (2010). A simple model for squirt-flow dispersion and attenuation in fluid-saturated granular rocks. *Geophysics*, 75(6), N109–N120. <https://doi.org/10.1190/1.3509782>
- Hashin, Z., & Shtrikman, S. (1963). A variational approach to the theory of the elastic behaviour of multiphase materials. *Journal of the Mechanics and Physics of Solids*, 11(2), 127–140. [https://doi.org/10.1016/0022-5096\(63\)90060-7](https://doi.org/10.1016/0022-5096(63)90060-7)
- He, Y., Rubino, J. G., Solazzi, S. G., Barbosa, N. D., Favino, M., Chen, T., et al. (2022). Numerical upscaling of seismic signatures of poroelastic rocks containing mesoscopic fluid-saturated voids. *Journal of Geophysical Research: Solid Earth*, 127(6), e2021JB023473. <https://doi.org/10.1029/2021JB023473>
- Horikawa, T., Katsura, M., Yokota, T., & Nakashima, S. (2021). Effects of pore water distributions on P-wave velocity–water saturation relations in partially saturated sandstones. *Geophysical Journal International*, 226(3), 1558–1573. <https://doi.org/10.1093/gji/ggab143>
- Hu, C., Tu, N., & Lu, W. (2013). Seismic attenuation estimation using an improved frequency shift method. *IEEE Geoscience and Remote Sensing Letters*, 10(5), 1026–1030. <https://doi.org/10.1109/LGRS.2012.2227933>
- Johnson, D. L. (1986). *Frontiers in physical acoustics: Recent developments in the acoustic properties of porous media*. Elsevier.
- Johnston, D. H., Toksöz, M. N., & Timur, A. (1979). Attenuation of seismic waves in dry and saturated rocks: II. Mechanisms. *Geophysics*, 44(4), 691–711. <https://doi.org/10.1190/1.1440970>
- Katz, A. J., & Thompson, A. H. (1985). Fractal sandstone pores: Implications for conductivity and pore formation. *Physical Review Letters*, 54(12), 1325–1328. <https://doi.org/10.1103/PhysRevLett.54.1325>
- Klimeš, L. (2002). Correlation functions of random media. In *Seismic waves in laterally inhomogeneous media* (pp. 1811–1831). Birkhäuser. https://doi.org/10.1007/978-3-0348-8146-3_22
- Krohn, C. E. (1988). Sandstone fractal and Euclidean pore volume distributions. *Journal of Geophysical Research*, 93(B4), 3286–3296. <https://doi.org/10.1029/JB093iB04p03286>
- Kuteynikova, M., Tisato, N., Jänicke, R., & Quintal, B. (2014). Numerical modeling and laboratory measurements of seismic attenuation in partially saturated rock. *Geophysics*, 79(2), L13–L20. <https://doi.org/10.1190/geo2013-0020.1>
- Lebedev, M., Toms-Stewart, J., Clennell, B., Pervukhina, M., Shulakova, V., Paterson, L., et al. (2009). Direct laboratory observation of patchy saturation and its effects on ultrasonic velocities. *The Leading Edge*, 28(1), 24–27. <https://doi.org/10.1190/1.3064142>
- Li, H., Chang, X., Xie, X.-B., & Wang, Y. (2022). Spatiotemporal variations in seismic attenuation during hydraulic fracturing: A case study in a tight oil reservoir in the Ordos Basin, China. *Geophysics*, 87(2), B69–B79. <https://doi.org/10.1190/geo2021-0013.1>
- Li, H., Wang, D., Gao, J., Zhang, M., Wang, Y., Zhao, L., & Yang, Z. (2020). Role of saturation on elastic dispersion and attenuation of tight rocks: An experimental study. *Journal of Geophysical Research: Solid Earth*, 125(4), e2019JB018513. <https://doi.org/10.1029/2019JB018513>
- Li, J., Hussaini, S. R., & Dvorkin, J. (2020). Permeability-porosity relations from single image of natural rock: Subsampling approach. *Journal of Petroleum Science and Engineering*, 194, 107541. <https://doi.org/10.1016/j.petrol.2020.107541>
- Li, X., Zhong, L., & Pyrak-Nolte, L. J. (2001). Physics of partially saturated porous media: Residual saturation and seismic-wave propagation. *Annual Review of Earth and Planetary Sciences*, 29(1), 419–460. <https://doi.org/10.1146/annurev.earth.29.1.419>
- Lopes, S., & Lebedev, M. (2012). Research note: Laboratory study of the influence of changing the injection rate on the geometry of the fluid front and on P-wave ultrasonic velocities in sandstone. *Geophysical Prospecting*, 60(3), 572–580. <https://doi.org/10.1111/j.1365-2478.2011.01009.x>
- Luo, C., Ba, J., & Guo, Q. (2023). Probabilistic seismic petrophysical inversion with statistical double-porosity Biot-Rayleigh model. *Geophysics*, 88(3), 1–54. <https://doi.org/10.1190/geo2022-0288.1>
- Ma, R., & Ba, J. (2020). Coda and intrinsic attenuations from ultrasonic measurements in tight siltstones. *Journal of Geophysical Research: Solid Earth*, 125(4), e2019JB018825. <https://doi.org/10.1029/2019JB018825>
- Ma, R., Ba, J., Carcione, J., Lebedev, M., & Wang, C. (2021). Experimental study on petrophysical properties as a tool to identify pore fluids in tight-rock reservoirs. *Frontiers in Earth Science*, 9, 652344. <https://doi.org/10.3389/feart.2021.652344>
- Ma, R., Ba, J., & Carcione, J. M. (2023). Frequency-dependent P-wave anelasticity due to multiscale (fractal) heterogeneities in rocks. *International Journal of Rock Mechanics and Mining Sciences*, 162, 105297. <https://doi.org/10.1016/j.ijrmmms.2022.105297>
- Mavko, G., & Nur, A. (1975). Melt squirt in the asthenosphere. *Journal of Geophysical Research*, 80(11), 1444–1448. <https://doi.org/10.1029/JB080i11p01444>
- Mikhailsevitch, V., Lebedev, M., & Gurevich, B. (2016). Laboratory measurements of the effect of fluid saturation on elastic properties of carbonates at seismic frequencies: Effect of fluid saturation on carbonates. *Geophysical Prospecting*, 64(4), 799–809. <https://doi.org/10.1111/1365-2478.12404>
- Mukhametdinova, A., Kazak, A., Karamov, T., Bogdanovich, N., Serkin, M., Melekhin, S., & Cheremisin, A. (2020). Reservoir properties of low-permeable carbonate rocks: Experimental features. *Energies*, 13(9), 2233. <https://doi.org/10.3390/en13092233>
- Müller, T. M., & Gurevich, B. (2004). One-dimensional random patchy saturation model for velocity and attenuation in porous rocks. *Geophysics*, 69(5), 1166–1172. <https://doi.org/10.1190/1.1801934>
- Müller, T. M., Gurevich, B., & Lebedev, M. (2010). Seismic wave attenuation and dispersion resulting from wave-induced flow in porous rocks — A review. *Geophysics*, 75(5), 147–164. <https://doi.org/10.1190/1.3463417>
- Müller, T. M., Toms-Stewart, J., & Wenzlau, F. (2008). Velocity-saturation relation for partially saturated rocks with fractal pore fluid distribution. *Geophysical Research Letters*, 35(9), L09306. <https://doi.org/10.1029/2007GL033074>
- Murphy, W. F. (1982). Effects of partial water saturation on attenuation in Massillon sandstone and Vycor porous glass. *Journal of the Acoustical Society of America*, 71(6), 1458–1468. <https://doi.org/10.1121/1.387843>
- O'Connell, R. J., & Budiansky, B. (1977). Viscoelastic properties of fluid-saturated cracked solids. *Journal of Geophysical Research*, 82(36), 5719–5735. <https://doi.org/10.1029/JB082i036p05719>
- Partyka, G. A., Thomas, J. B., Turco, K. P., & Hartmann, D. J. (2000). Upscaling petrophysical properties to the seismic scale. In *SEG technical program expanded abstracts* (pp. 1636–1638). <https://doi.org/10.1190/1.1815729>
- Pei, F., Zou, C., He, T., Pan, L., Xiao, K., Shi, G., & Ren, K. (2011). Experimental study of the relationship between fluid density and saturation and sonic wave velocity of rock samples from the WXS Depression, South China Sea. *Petroleum Science*, 8(1), 43–48. <https://doi.org/10.1007/s12182-011-0113-5>

- Pride, S. R., & Berryman, J. G. (2003). Linear dynamics of double-porosity dual-permeability materials. II. Fluid transport equations. *Physical Review E*, 68(3), 036604. <https://doi.org/10.1103/PhysRevE.68.036604>
- Pride, S. R., & Masson, Y. J. (2006). Acoustic attenuation in self-affine porous structures. *Physical Review Letters*, 97(18), 184301. <https://doi.org/10.1103/PhysRevLett.97.184301>
- Sams, M. S., Neep, J. P., Worthington, M. H., & King, M. S. (1997). The measurement of velocity dispersion and frequency-dependent intrinsic attenuation in sedimentary rocks. *Geophysics*, 62(5), 1456–1464. <https://doi.org/10.1190/1.1444249>
- Sokama-Neuyam, Y. A., Boakye, P., Aggrey, W. N., Obeng, N. O., Adu-Boahene, F., Woo, S. H., & Ursin, J. R. (2020). Theoretical modeling of the impact of salt precipitation on CO₂ storage potential in fractured saline reservoirs. *ACS Omega*, 5(24), 14776–14785. <https://doi.org/10.1021/acsomega.0c01687>
- Spencer, J. W., & Shine, J. (2016). Seismic wave attenuation and modulus dispersion in sandstones. *Geophysics*, 81(3), D211–D231. <https://doi.org/10.1190/geo2015-0342.1>
- Subramaniyan, S., Quintal, B., Madonna, C., & Saenger, E. H. (2015). Laboratory-based seismic attenuation in Fontainebleau sandstone: Evidence of squirt flow. *Journal of Geophysical Research: Solid Earth*, 120(11), 7526–7535. <https://doi.org/10.1002/2015JB012290>
- Sun, X., Tang, X., Cheng, C. H., (Arthur), & Frazer, L. N. (2000). P- and S-wave attenuation logs from monopole sonic data. *Geophysics*, 65(3), 755–765. <https://doi.org/10.1190/1.1444774>
- Toksöz, M. N., Johnston, D. H., & Timur, A. (1979). Attenuation of seismic waves in dry and saturated rocks: I. Laboratory measurements. *Geophysics*, 44(4), 681–690. <https://doi.org/10.1190/1.1440969>
- Toms, J., Müller, T. M., & Gurevich, B. (2007). Seismic attenuation in porous rocks with random patchy saturation. *Geophysical Prospecting*, 55(5), 671–678. <https://doi.org/10.1111/j.1365-2478.2007.00644.x>
- Wang, Y.-R., Zong, Z.-Y., & Sun, Q.-H. (2023). Modeling the effect of multiscale heterogeneities on wave attenuation and velocity dispersion. *IEEE Transactions on Geoscience and Remote Sensing*, 61, 1–17. <https://doi.org/10.1109/TGRS.2023.3244654>
- Wang, Y.-R., Zong, Z.-Y., & Yin, X.-Y. (2022). Fluid discrimination incorporating amplitude variation with angle inversion and squirt flow of the fluid. *Petroleum Science*, 19(4), 1592–1604. <https://doi.org/10.1016/j.petsci.2022.03.007>
- Wei, Q., Wang, Y., Han, D., Sun, M., & Huang, Q. (2021). Combined effects of permeability and fluid saturation on seismic wave dispersion and attenuation in partially-saturated sandstone. *Advances in Geo-Energy Research*, 5(2), 181–190. <https://doi.org/10.46690/ager.2021.02.07>
- Wei, Y., Ba, J., Carcione, J. M., Fu, L.-Y., Pang, M., & Qi, H. (2021). Temperature, differential pressure, and porosity inversion for ultradeep carbonate reservoirs based on 3D rock-physics templates. *Geophysics*, 86(3), M77–M89. <https://doi.org/10.1190/geo2020-0550.1>
- White, J. E. (1975). Computed seismic speeds and attenuation in rocks with partial gas saturation. *Geophysics*, 40(2), 224–232. <https://doi.org/10.1190/1.1440520>
- Winkler, K. W. (1985). Dispersion analysis of velocity and attenuation in Berea sandstone. *Journal of Geophysical Research*, 90(B8), 6793–6800. <https://doi.org/10.1029/JB090iB08p06793>
- Winkler, K. W., & Nur, A. (1979). Pore fluids and seismic attenuation in rocks. *Geophysical Research Letters*, 6(1), 1–4. <https://doi.org/10.1029/GL006i001p00001>
- Winkler, K. W., & Nur, A. (1982). Seismic attenuation: Effects of pore fluids and frictional-sliding. *Geophysics*, 47(1), 1–15. <https://doi.org/10.1190/1.1441276>
- Winkler, K. W., Nur, A., & Gladwin, M. (1979). Friction and seismic attenuation in rocks. *Nature*, 277(5697), 528–531. <https://doi.org/10.1038/277528a0>
- Xie, J.-Y., Zhang, J.-J., Xiang, W., Fang, Y.-P., Xue, Y.-J., Cao, J.-X., & Tian, R.-F. (2022). Effect of microscopic pore structures on ultrasonic velocity in tight sandstone with different fluid saturation. *Petroleum Science*, 19(6), 2683–2694. <https://doi.org/10.1016/j.petsci.2022.06.009>
- Xu, M., Yin, X., & Zong, Z. (2022). Wave dispersion and attenuation due to multi-scale wave-induced fluid flow in layered partially saturated pore-crack media. *Journal of Petroleum Science and Engineering*, 208, 109447. <https://doi.org/10.1016/j.petrol.2021.109447>
- Xu, Y., Li, Q., & King, H. E. (2017). Modeling oil recovery for mixed macro- and micro-pore carbonate grainstones. *Scientific Reports*, 7(1), 9780. <https://doi.org/10.1038/s41598-017-09507-4>
- Yang, Z.-Q., He, T., & Zou, C.-C. (2020). A dynamic elastic model for squirt-flow effect and its application on fluid-viscosity-associated velocity dispersion in reservoir sandstones. *Geophysics*, 85(4), MR201–MR212. <https://doi.org/10.1190/geo2019-0312.1>
- Yin, C.-S., Batzle, M. L., & Smith, B. J. (1992). Effects of partial liquid/gas saturation on extensional wave attenuation in Berea sandstone. *Geophysical Research Letters*, 19(13), 1399–1402. <https://doi.org/10.1029/92GL01159>
- Yu, B., & Li, J. (2001). Some fractal characters of porous media. *Fractals*, 09(03), 365–372. <https://doi.org/10.1142/S0218348X01000804>
- Yurikov, A., Lebedev, M., & Pervukhina, M. (2018). Ultrasonic velocity measurements on thin rock samples: Experiment and numerical modeling. *Geophysics*, 83(2), MR47–MR56. <https://doi.org/10.1190/geo2016-0685.1>
- Zhang, C., & Ulrych, T. J. (2002). Estimation of quality factors from CMP records. *Geophysics*, 67(5), 1542–1547. <https://doi.org/10.1190/1.1512799>
- Zhang, L., Ba, J., Carcione, J. M., & Fu, L. (2020). Differential poroelasticity model for wave dissipation in self-similar rocks. *International Journal of Rock Mechanics and Mining Sciences*, 128, 104281. <https://doi.org/10.1016/j.ijrmmms.2020.104281>
- Zhang, L., Ba, J., Carcione, J. M., & Wu, C. (2022). Seismic wave propagation in partially saturated rocks with a fractal distribution of fluid-patch size. *Journal of Geophysical Research: Solid Earth*, 127(2), e2021JB023809. <https://doi.org/10.1029/2021JB023809>
- Zhao, L., Tang, G., Sun, C., Zhao, J., & Wang, S. (2021). Dual attenuation peaks revealing mesoscopic and microscopic fluid flow in partially oil-saturated Fontainebleau sandstones [Dataset]. *Geophysical Journal International*, 224(3), 1670–1683. <https://doi.org/10.1093/gji/ggaa551>
- Zhong, Z., Chen, Y., Fu, M., Li, M., Yang, K., Zeng, L., et al. (2023). Role of CO₂ geological storage in China's pledge to carbon peak by 2030 and carbon neutrality by 2060. *Energy*, 272, 127165. <https://doi.org/10.1016/j.energy.2023.127165>
- Zhubayev, A., Houben, M. E., Smeulders, D. M. J., & Barnhoorn, A. (2016). Ultrasonic velocity and attenuation anisotropy of shales, Whitby, United Kingdom. *Geophysics*, 81(1), D45–D56. <https://doi.org/10.1190/geo2015-0211.1>